Solid Earth Discuss., https://doi.org/10.5194/se-2019-28
Manuscript under review for journal Solid Earth
Discussion started: 14 February 2019

Solid Earth Discussions

Deformation mechanisms in mafic amphibolites and granulites: record from the Semail metamorphic sole during subduction infancy

Mathieu Soret[1], Philippe Agard[1], Benoît Ildefonse[2], Benoît Dubacq[1], Cécile Prigent[3], Claudio Rosenberg[1]

[1] Sorbonne Université, CNRS-INSU, Institut des Sciences de la Terre Paris, ISTeP UMR 7193, F-75005 Paris, France
[2] Géosciences Montpellier, Univ. Montpellier, CNRS, Univ. Antilles, 34095, Montpellier, cedex, 05, France
[3] Univ. Grenoble Alpes, Univ. Savoie Mont Blanc, CNRS, IRD, IFSTTAR, ISTerre, 38000 Grenoble, France

Correspondence to: Mathieu Soret (math.soret@gmail.com)

Abstract. This study sheds light on the deformation mechanisms of subducted mafic rocks metamorphosed at amphibolite and granulite facies conditions, and on their importance for strain accommodation and localization at the top of the slab during subduction infancy. These rocks, namely metamorphic soles, are oceanic slivers stripped from the downgoing slab and plastered below the upper plate mantle wedge during the first million years of intra-oceanic subduction, when the subduction interface is still warm. Their formation and intense deformation (i.e. shear strain ≥ 5) attest to a systematic and transient coupling between the plates over a restricted time span of ~1 My and specific rheological conditions. Combining micro-structural analyses with mineral chemistry constrains grain-scale deformation mechanisms and the rheology of amphibole and amphibolites along the plate interface during early subduction dynamics, as well as the interplay between brittle and ductile deformation, water activity, mineral change, grain size reduction and phase mixing. Results indicate, in particular, that increasing pressure-temperature conditions and slab dehydration (from amphibolite to granulite facies) lead to the crystallization of mechanically strong phases (garnet, clinopyroxene and high-grade amphibole) and rock hardening. In contrast, during early exhumation and cooling (from ~850 down to ~700°C – 0.7 GPa), the garnet-clinopyroxene-bearing amphibolite experiences pervasive retrogression (and fluid ingression) and significant strain weakening essentially accommodated by dissolution-precipitation and grain boundary sliding processes. Observations also indicate cyclic brittle deformation near peak conditions and throughout the early exhumation, which contributed to fluid channelization within the amphibolites, and possibly strain localization accompanying detachment from the slab. These mechanical transitions, coeval with detachment and early exhumation of the HT metamorphic soles, controlled mechanical coupling across the plate interface during subduction infancy, between the top of the slab and the peridotites above. Our findings may thus apply to other geodynamic environments where similar temperatures, lithologies, fluid circulation and mechanical coupling between mafic rocks and peridotites prevail, such as in mature warm subduction zones (e.g., Nankai, Ca dia), in lower continental crust shear zones and oceanic detachments.

1 Introduction

Metamorphic soles underlying ophiolites are 10-100 m thick metamorphosed oceanic slivers stripped from the slab during subduction infancy (Hacker, 1990; Dewey and Casey, 2013; Agard et al., 2016; Rioux et al., 2016; Guilmette et al., 2018).

Solid Earth Discuss., https://doi.org/10.5194/se-2019-28
Manuscript under review for journal Solid Earth
Discussion started: 14 February 2019

They get accreted to the upper plate mantle wedge (i.e., the future ophiolite; Fig. 1a) due to the rheology of the nascent, still warm interface, which favours strong mechanical coupling between the two plates (Agard et al., 2016, 2018; Soret et al., 2016, 2017). Changes in lithologies and metamorphic conditions indicate short-lived, stepwise accretion at characteristic pressure-temperature-time (P–T–t) conditions (Wakabayashi and Dilek, 2000, 2003; Plunder et al., 2016; Soret et al., 2017): two major accretion events have been identified in the mafic, high-temperature amphibolite to granulite facies portions of the Semail ophiolite sole (Oman, and United Arab Emirates; UAE), at 850 ± 50°C – 0.9 ± 0.2 GPa and 750 ± 50°C – 0.7 ± 0.2 GPa (Soret et al., 2 The striking similarity of P–T conditions across the whole ophiolite width (~150 km) also indicates that these slivers experienced large shear strains of at least >4–5 gamma during accretion/exhumation (Soret et al., 2017), coeval with large ductile deformation in the banded perido bove (Boudier et al., 1988; Prigent et al., 2018a,c).

How deformation is accommodated within the amphibole-bearing sole rocks, and how mafic slivers get detached from the top of the subducting slab and accreted to the upper plate at T ≥700°C remains unknown. To investigate the deformation mechanisms accompanying the progressive change of P–T conditions and mineralogy (i.e., essentially amphibole, with varying amounts of plagioclase, clinopyroxene and garnet), we provide detailed micro-structural and mineral chemistry data from the well-constrained Oman–UAE example. In contrast to plagioclase and clinopyroxene (e.g., Bascou et al., 2002; Dimanov et al., 2007; Hier-Majumder et al., 2005; Rybacki and Dresen, 2004), the physical properties and mechanical behaviour of amphibole and amphibole-bearing polymineralic aggregates, commonly found over a large range of P–T and water activity conditions, have been far less studied and remain puzzling (see Getsinger and Hirth, 2014). Understanding these deformation mechanisms is therefore expected to shed light on the plate interface rheology during subduction infancy (Soret et al., 2016, 2017; Prigent et al., 2018b) or beneath warm subduction zones (where similar temperatures, lithologies and mechanical coupling are expected at ~60 km depth; Abers et al., 2017), as well as on the rheological behaviour of amphibole-bearing rocks and strain localization in mid-crustal environments (e.g., continental crust: Getsinger et al., 2013; Giuntoli et al., 2018; Imon et al., 2004; Tatham et al., 2008; oceanic detachment faults or transform faults : Boschi et al., 2006; Escartín et al., 2003).

2 Deformation of amphibolites

Naturally and experimentally deformed amphibolites commonly show well-developed foliation and strong crystal–preferred orientation (CPO), regardless of their P–T–water activity conditions and compositional range. Foliation is usually underlined by the shape–preferred orientations (SPO) of amphibole and plagioclase (e.g., Cao et al., 2010; Getsinger et al., 2013; Imon et al., 2004; Ko and Jung, 2015; Tatham et al., 2008). Compared to plagioclase and clinopyroxene, the CPO of amphibole is generally stronger (Cao et al., 2010; Diaz Aspiroz et al., 2007; Getsinger and Hirth, 2014; Getsinger et al., 2013; Gómez Barreiro et al., 2010; Imon et al., 2004; Kim et al., 2015; Ko and Jung, 2015, Siegesmund et al., 1994; Tatham et al., 2008), hence leading several authors to consider that it accounts for seismic anisotropy in the lower/middle crust (Ji et al., 2013; Lloyd et al., 2011; Mainprice and Nicolas, 1989; Tatham et al., 2008) and in subduction zones (Ko and Jung, 2015).

Solid Earth Discuss., https://doi.org/10.5194/se-2019-28
Manuscript under review for journal Solid Earth
Discussion started: 14 February 2019

There are different interpretations for the strong CPO of amphibole and its SPO. The presence of a CPO usually hints at dislocation creep as the dominant deformation mechanism (e.g., Wenk and Christie, 1991). Several studies report intra-crystalline deformation in amphibole at high temperature (T ≥ 650–700˚C), compatible with dislocation glide along the most favourable slip systems {hk0}[001] (Berger and Stünitz, 1996; Diaz Aspiroz et al., 2007; Cao et al., 2010; Gomez Barreiro et al., 2010). However, other studies have suggested that amphibole is one of the strongest silicates, with limited ability to deform by dislocation creep (e.g., Brodie and Rutter, 1985). Amphibole would rather behave as a rigid particle, rotating and fracturing (Berger and Stünitz, 1996; Hacker and Christie, 1990; Ildefonse et al., 1990; Imon et al., 2004, Nyman et al, 1992; Ko and Jung, 2015; Shelley, 1994), and/or dissolving and reprecipitating during deformation (Berger and Stünitz, 1996; Brodie, 1981; Guintoli et al., 2018; Hacker and Christie, 1990; Imon et al., 2004; Kruse and Stünitz, 1999; Marti et al., 2017). While variations in P–T conditions, water activity and grain size are known to control the activation of the different deformation mechanisms (e.g., Brodie and Rutter, 1985), their respective roles has not been clearly assessed in the specific case of amphibole.

3 The Semail metamorphic sole

The Semail metamorphic sole is a relatively thin unit (commonly ≤ 100 m thick) found at the base of the ≥ 10 km thick Semail ophiolite (Oman and UAE; Fig. 1a-c). This unit results from the juxtaposition of several slices of oceanic crust (Fig. 1c-d; Soret et al., 2017 and references therein) that were buried, strained and metamorphosed against the hot overlying mantle wedge, from granulite-facies (for the uppermost slice) to upper greenschist facies conditions (for the lowermost one). In practice, it is convenient to distinguish in the field a high-temperature (HT) sole, found directly below the mylonitic basal peridotite, from a low-temperature (LT) sole onto which it is thrust. This structural organization is found all along the Semail ophiolite (Fig. 1b-c; Gnos, 1998), from Wadi Tayin (Oman) in the south to Sumeini (Oman) and Asimah–Khubakhib (UAE) in the north. These characteristics are common to most metamorphic soles worldwide, regardless of the nature of the overlying ophiolite (see Agard et al., 2016).

The HT sole is composed of two major sub-units (Fig. 1c), being either made of garnet–clinopyroxene amphibolites (HTa, above) or plagioclase-rich amphibolites (HTb, below). The contrasting Ti content of amphibole, which correlates positively with crystallization temperature (Ernst and Liu, 1998) and shows a stepwise decrease from ≥ 0.2 a.p.f.u. (atoms per formula unit) in HTa to ≤ 0.15 a.p.f.u. in HTb (Fig. 1e; Soret et al., 2017), indicates a ~100˚C gap in peak T between both units. Mapping of the Ti-content is used hereafter to track different amphibole generations (Sect. 5.3).

Peak P–T conditions for the HT sole were estimated at 850 ± 50˚C – 0.9 ± 0.1 GPa for HTa and 725 ± 50°C – 0.8 ± 0.1 GPa for HTb (Fig. 1f; see Soret et al., 2017, for details). The preservation of prograde chemical zoning (over a dT ≥ 100˚C and a dP ≥ 0.1 GPa) suggests fast exhumation of the HT sole after reaching peak conditions (≤ 1–2 Ma), as supported by radiometric dating (e.g., Hacker, 1990; Rioux et al., 2016; Guilmette et al., 2018).

Solid Earth Discuss., https://doi.org/10.5194/se-2019-28
Manuscript under review for journal Solid Earth
Discussion started: 14 February 2019

The underlying LT sole (Fig. 1c) is mainly composed of greenschist facies metacherts, with imbrications of amphibole-bearing metatuffs, and is not considered here. Estimated peak P–T conditions are more loosely constrained at 530 ± 50°C – 0.5 ± 0.1 GPa (Fig. 1f; Soret et al., 2017).

The entire metamorphic sole shows a strong planar fabric (Figs. 2a-c) with evidence of both pure and simple shear deformation. In the LT sole, the lattice preferred orientation of quartz in the inter-bedded quartzite is consistent with shear senses observed in the basal banded peridotite (Ambrose et al., 2018; Boudier et al., 1988; Gray et Gregory, 2000). Deformation is less conspicuous in the garnet–clinopyroxene-bearing HTa sole compared to the HTb and LT soles, in which larger lithological heterogeneities exist. HTa amphibolite is indeed homogeneous (Figs. 1c, 2a-b), fine-grained and composed of Amp+Grt+Cpx±Pl, while HTb amphibolite is coarser-grained and consists of Amp+Pl±Ep with rare biotite-plagioclase-rich imbricated layers (Figs. 1c, 2c).

4 Methods and sampling strategy

A suite of samples was collected from the two sub-units of the HT sole from three localities where the HT sole is the most complete and best preserved (Khubakhib, Sumeini and Wadi Tayin; Fig. 1b). Six samples (five from HTa and one from HTb; Fig. 1c, Table 1) were analysed using electron back-scattered diffraction (EBSD). For clarity, only microstructures of the most complete and representative section (the three HTa unit samples from Sumeini; see Soret et al., 2017) are detailed here. Microstructural descriptions for the Khubakhib and Wadi Tayin sections are given as supplementary information.

EBSD data were collected using a CamScan X500FE CrystalProbe scanning electron microscope (SEM) at Géosciences Montpellier (France). Measurements were performed on polished thin sections at a 25 mm working distance with an accelerating voltage of 15 kV. For each sample (see map step size in Table 1), amphibole, plagioclase, clinopyroxene, garnet (together with prehnite, epidote and Ti-rich phases such as rutile, titanite and ilmenite) were indexed wherever present. Resulting maps were first filtered using the Channel 5 software suite (Schmidt and Olesen, 1989) to increase the quality of the maps. Isolated pixels were removed, and non-indexed pixels with a minimum of 6 identical neighbours were filled with the same orientation. Maps were then processed using MTEX, a MATLAB toolbox for textural analysis (Bachmann et al., 2010; Hielscher and Schaeben, 2008; Mainprice et al., 2014).

In MTEX, misorientation angles (defined as the lowest rotation angle between two pixels about a common axis that brings two lattices into parallelism; e.g., Lloyd et al., 1997; Wheeler et al., 2001) were used to identify grain boundaries, applying a 10° threshold between adjacent pixels. Grains with a surface smaller than 10 pixels were discarded. Twins in plagioclase were distinguished from grain boundaries by filtering out the 178° to 180°misorientations during grain boundary identification. Pole figures were calculated using the crystallographic orientation of each grain. All plots are represented in lower hemisphere projections in the specimen reference frame, with contours as multiples of a uniform distribution. Mineral crystallographic

Solid Earth Discuss., https://doi.org/10.5194/se-2019-28
Manuscript under review for journal Solid Earth
Discussion started: 14 February 2019

preferred orientation (CPO) strength was characterized using the J index (from 1 in the case of random orientation distribution to infinity in the case of an ideal single crystal; Bunge, 1982), calculated from the orientation distribution function (ODF; Mainprice et al., 2014). The shape preferred orientation (SPO) was calculated from the average orientation of the longest-axis of each grain and the aspect ratio (AR) of grains is the length ratio en the principal axes of the best-fit ellipse. Kernel Average Misorientation (KAM) analysis used to map intragranular misorientations in clinopyroxene, plagioclase and amphibole. The is defined as the average misorientation around a measurement point with respect to the 16 nearest neighbour points in a particular grain.

To track nucleation/recrystallization processes during the deformation of amphibole and amphibolites, composition maps (Fig. 6) were acquired with 1–2 µm spatial resolution (at the exception of the one map acquired with a 10 µm step size; Fig. 6m). Major elements were measured at CAMPARIS (Sorbonne Univ.) and at ISTO (Univ. Orléans, France) using a CAMECA SX-5 electron microprobe. Classical analytical conditions were used (200 kV, 40 nA, wavelength-dispersive spectroscopy mode), using Fe2O3 (Fe), MnTiO3 (Mn, Ti), diopside (Mg, Si), orthoclase (Al, K), anorthite (Ca) and albite (Na) as standards. See Soret et al. (2017) for representative point analyses of garnet, amphibole, clinopyroxene, feldspar and epidote in these samples.

Mineral abbreviations used throughout the text and figures are given after Whitney and Evans (2010).

5 Results

5.1 Sample overview

Samples from the Sumeini HTa unit are presented structurally from top to bottom, starting from the highest-grade samples collected near the contact with the overlying peridotite to garnet-free samples away from the contact. Mineral occurrences and proportions are detailed in Table 1.

Within 2.5 m from the peridotite, the metamorphic sole is composed of a garnet-clinopyroxene bearing amphibolite. Peak metamorphic t s are well preserved in sample SE13-67 (Fig. 2d). T net-clinopyroxene amphibolite SE13-67 exhibits a mylonitic foliation, locally transected at a relatively low angle (15–25°C) by C'-type bands indicating a dextral shear sense in the thin-section frame. The foliation comprises fine-grained aggregates of brown amphibole and clinopyroxene, and locally garnet and clinopyroxene porphyroclasts (Fig. 2d). Three disjunctive domains are distinguished in thin section:

- Area 1 is dominantly composed of a clinopyroxene aggregate aligned in the foliation, and is cut across at low angle by veins of epidote ± prehnite ± apatite (Figs. 2d, 3a).
- Area 2 (a, b) is composed of amphibole (50–65%) and clinopyroxene (25–35%) (Figs. 2d, 3b,c).
- Area 3 is composed of amphibole (42%), clinopyroxene (22%) and garnet (12%) (Figs. 2d, 3d).

Solid Earth Discuss., https://doi.org/10.5194/se-2019-28
Manuscript under review for journal Solid Earth
Discussion started: 14 February 2019

Plagioclase is either rare or absent in the matrix, and most crystals have not been successfully indexed due to pervasive late sericitization by a minute assemblage of Ab+Ep+Ms. Epidote (≤ 2 vol.%), apatite (≤1 vol.%) and prehnite (≤5%), commonly found in veins sub-parallel to the foliation (Fig. 2d), testify to a late stage of deformation and (Ca-rich) fluid circulation at low-T conditions (≤ 700˚C), which is documented across the entire HT metamorphic sole (Fig. 2b; Soret et al., 2017).

The degree of high-T (700–800°C) retrogression increases steadily towards the base of the HTa unit, and is maximum at the contact with the HTb unit. Rocks located further away from the sole-peridotite contact therefore mostly record lower temperature, post-T-peak deformation. About 8 m the peridotite (sample SE13-69; Fig. 4a), the metamorphic sole exhibits a coarser-grained, more conspicuous foliation characterized by higher proportions of brown amphibole (58%) and plagioclase (14%), partly replacing clinopyroxene (12%) and garnet (3%). About 25 m below the contact (sample SE13-76; Fig. 4b), garnet and clinopyroxene no longer coexist in the metamorphic sole. Amphibole (23%) has a brown to greenish-brown colour and is closely associated with plagioclase (64%), both with coarser grain size. Amphibole grains do not commonly form aggregates. They are more scattered in the plagioclase-rich matrix. The amphibolite is also strongly affected by the crystallization of yellowish epidote (12%), usually aligned along C'-type shear bands together with fine-grained amphibole.

The underlying HTb unit is made of coarse-grained (typically 1 mm in diameter) plagioclase and greenish-brown amphibole aggregates, roughly in equal proportions, rare ≤50 cm-thick intercalations of biotite-plagioclase-rich amphibolite. Plagioclase-rich and darker amphibole-rich layers alternate throughout this unit (Fig. 2c).

5.2 Microstructures

5.2.1 Amphibole

The amphibole average grain size decreases towards the contact with the peridotite (Table 1; Figs. S1a-c), i.e. where peak-metamorphic textures are best-preserved (≤ 2.5 m; SE13-67). In this sample, the average grain size for amphibole associated with clinopyroxene (A2) ilar to that for amphibole associated with clinopyroxene and garnet (A3; 75 ± 50 µm, 65 ± 50 µm, respectively; Figs. 5b-c; Table 1). Most amphibole grains have a subhedral shape (Fig. 5a). Away from the peridotite, the amphibole average grain size and its standard deviation increase with increasing retrogression from 115 ± 75 µm (at 8 m; SE13-69; Fig. 5d) to 160 ± 120 µm (at 25m; SE13-76; Fig. 5e), and the shape becomes more anhedral. The mean aspect ratio of amphibole (1.9 ± 0.6) does not vary with the distance from the peridotite nor with the mineral assemblage (Fig. S1b). Amphibole SPO, subparallel to the shear plane, is very strong in all samples and its intensity correlates positively with grain size and aspect ratio (Fig. S1a-b).

Solid Earth Discuss., https://doi.org/10.5194/se-2019-28
Manuscript under review for journal Solid Earth
Discussion started: 14 February 2019

Large amphibole grains display intragranular fractures and irregular boundaries in all samples, especially where bounded by -altered- plagioclase or prehnite (Figs. 5a-d). Some fractures are parallel to cleavage planes, while others are parallel or perpendicular to the [001] direction (Fig. 5a-b). These fractures locally dissect the large grains, forming smaller grains with straight and sharp intra-phase boundaries (Fig. 5a). Later and wider prehnite-filled fractures are also found transecting the amphibolite (Fig. 5c).

In the HTa unit, only rare (< 5%) amphibole grains show microstructural evidence for intra-crystalline plasticity, as undulatory or patchy extinction (Fig) and subgrain boundaries, and their proportion increases in the more retrogressed samples (closer to the contact with the HTb unit; Fig. 6c-d). In the sample best-preserved from retrogression (SE13-67), while the Kernel Average Misorientation (KAM) maps outline the presence of intracrystalline misorientations in most amphibole grains, most of these misorientations are associated with only small rotations (≤ 3 g. 6e-i). Grains with higher misorientation angles are those with the highest micro-fracture density (white arrows; Fig. 6a,e). In the more retrogressed samples (SE13-69, SE13-76), amphibole grains show a lower density of micro-fractures (Fig. 6b-d). In sample S 9, intragranular misorientations are rare in amphibole (Fig. 6f), while in sample (SE13-76) they are much more common. In both samples, these misorientations are spatially correlated with undulatory extinction and subgrain formation (Fig. 6b-i), especially in the largest and/or most elongated amphibole grains (i.e., which can locally show intragranular fractures; Fig. 6c-d).

5.2.2 Garnet

Garnet grains have rounded to ellipsoidal shapes (Figs. 2d, 5b-c) and essentially form σ-type porphyroclasts indicating a sense of shear consistent with that of fish-shaped amphibole (Figs. 2d, 5b). Strain shadows are composed of fine-grained amphibole and clinopyroxene. In places, garnet crystals are fractured (Fig. 5c). These fractures cut across their prograde growth zonation (Soret et al., 2017) and are filled with foliated, fine-grained mixtures of amphibole + clinopyroxene ± rare plagioclase (Fig. 5c). Where retrogression is more pervasive (SE13-69), garnet is rimmed by plagioclase (Figs. 4a, 5d) and lacks of pressure shadows.

5.2.3 Clinopyroxene

Clinopyroxene grains have rounded to ellipsoidal shapes (Figs. 2d, 5f-h). The aspect ratio of clinopyroxene is smaller than that of amphibole (1.6 ± 0.4 on average) and does not vary with grain size, mineral assemblage or with the distance of the samples to the peridotite contact (Fig Like amphibole, clinopyroxene s are usually aligned in the foliation plane (Figs. 2d, 5b,g) but their SPO and its correlation with both grain size and aspect ratio are much weaker (Fig. S2f).

Within mono-mineralic layers (A1 in SE13-67; Figs. 2d, 3a the average grain size for clinopyroxene is 100 ± 70 µm (Fig. . Where associated with amphibole (A2 in SE13-67; Figs. 2d, 3b-c, 5g), clinopyroxene forms σ-type yroclasts with well-developed core-and-mantle structures indicating recrystalliz by subgrain rotation (Fig. 5g-h). The core shows

Solid Earth Discuss., https://doi.org/10.5194/se-2019-28
Manuscript under review for journal Solid Earth
Discussion started: 14 February 2019

undulose extinction while the mantle of dynamically recrystallized clinopyroxene (orange arrows; Fig. forms extensive tails indicating dextral sense of shear in the thin-section frame (Fig. 2d). Some new, recrystallized clinopyroxene grains display narrow and straight deformation twins. Small amphibole grains (green arrows; Fig. 5g-h), randomly oriented, are generally found along grain boundaries of newly recrystallized clinopyroxene grains (orange arrows; Figs. 5g-h).

Where garnet is present (A3 in SE13-67), clinopyroxene grains form fine-grained aggregates embedded in an amphibole-rich matrix (Fig 5b). However, the degree of phase mixing with amphibole in the matrix is higher than in Area 2. In both areas (A2 and A3), the average grain size (65±45 µm) is close to that of amphibole and smaller than in the monomineralic layer (A1; Fig .

Clinopyroxene porphyroclasts also show trails of secondary fluid inclusions that represent healed fluid-filled micro-fractures (dashed white arrows; Fig. 5h). Locally, minute amphibole can be found along these micro-fractures (white arrows; Fig. 5h). These narrow trails are continuous across the core of the porphyroclasts and usually disappear within the mantle, suggesting that fracturing preceded dynamic recrystallization. These trails are also locally cut across by the wider, white, prehnite-filled fractures.

5.2.4 Plagioclase

Plagioclase is rare, even in the best-preserved metamorphic sole samples. The analysis of CPO in plagioclase grains is complicated by retrogression, therefore the results shown below are restricted to the best-preserved grains, and may not be representative of all grains formed at high P–T.

5.3 Amphibole composition mapping

Amphibole composition plots within the pargasite to actinolite fields (see Soret et al. (2017) for detailed analyses). Hereafter, amphibole is referred to as Ti-high (≥ 0.2 a.p.f.u.), Ti-medium (0.1–0.2 a.p.f.u.) and Ti-low (≤ 0.1 a.p.f.u.) amphibole.

In sample SE13-67, amphibole grains show an homogeneous Ti-high composition (Fig. 6j-k), confirming that these grains formed at or near peak conditions. In the samples marked by a higher degree of retrogression at amphibolite-facies conditions (SE13-69; SE13-76), amphibole grains evidence a much more complex and patchy zoning pattern, with smaller Ti-rich areas than in sample SE13-67. These Ti-rich areas are usually truncated by Ti-medium to Ti-low areas, especially along micro-fractures (red arrows; Figs). In addition t rystallization of secondary plagioclase and ilmenite at amphibole lobate grain boundaries and/or along the micro-fractures (Fig. 6a-c), these zoning patterns indicate dissolution-precipitation during cooling (i.e., 800–700°C). Moreover, they support the obser that Ti-medium and Ti-low amphibole grains are not in equilibrium with clinopyroxene and garnet but rather with pla se.

Solid Earth Discuss., https://doi.org/10.5194/se-2019-28
Manuscript under review for journal Solid Earth
Discussion started: 14 February 2019

5.4 Crystallographic preferred orientation

5.4.1 Amphibole

In samples SE13-67 and SE13-69, where amphibole forms the load-bearing framework, it has a very strong CPO, with [001] axes (i.e., shortest Burgers vector; Hacker and Christie, 1990) mostly parallel to the lineation (Figs. 7a, 8a-c). Poles to (100) are subperpendicular to the foliation and poles to (010) are in the foliation, subperpendicular to the lineation (Fig. 7a). Poles to (100) always show the highest density and poles to (010) usually display the weakest preferred orientation. In the most retrogressed sample (SE13-76), poles to (010) and [001] are evenly distributed as girdles within the foliation plane (Figs. 7a, S5a).

Amphibole J-index ranges from 2.86 in the sample SE13-76 to 5.27 in the sample SE13-67 (Fig. 9a-b). The CPO strength is slightly positively correlated with the modal proportion of amphibole but no systematic correlation is found with the distance to the peridotite (Fig. 9a-b). In sample SE13-67, the CPO strength is significantly weakened around garnet and clinopyroxene porphyroclasts which show strong foliation deflection. In the more retrogressed sample SE13-69, where garnet and clinopyroxene coexist but do not deflect the foliation plane, amphibole has a strong CPO fabric (J-index = 3.67; Fig. 9a-b) as in the garnet-free layers of SE13-67. The weakest CPO (J-index=2.87; Fig. 9a-b) is observed away from the contact in the garnet-free sample SE13-76 which has the smallest amphibole modal proportion and the highest degree of retrogression. Moreover, as highlighted with the SPO, amphibole grains with smaller grain size (< 80 μm) and/or aspect ratio (< 1.5) display a similar CPO pattern but significantly weaker in intensity compared to larger or more elongate grains (Fig. 9c).

The misorientation angle distribution of amphibole in all samples highly differs from the theoretical random distribution (i.e., the "uniform" green curve; Fig. 7b). This is consistent with the strong intensity of amphibole CPO. Small misorientation angles (from 2 to 10°) are largely dominant. They correspond to rotations around the [001] axis, and to a much lesser extent around the [010] axis (Fig. 7c). The [010] axis concentration is slightly higher in sample SE13-76 compared to the other samples.

5.4.2 Clinopyroxene

Clinopyroxene has a moderate to weak CPO. As in amphibole, the [001] maximum is subparallel to the lineation but slightly more dispersed (Fig. 8d-f, 10a, S5b). The majority of CPO patterns has girdle concentrations of both (100) and (010) poles, except in sample SE13-69 where poles to (010) have a maximum normal to the foliation (Fig. 10a). In SE13-67, the strongest CPO (or J-index) is found within monomineralic layers of SE13-67 (J-index=2.61 in A1; Figs. 9a). In poly-mineralic aggregates, clinopyroxene J-index ranges from 1.21 to 1.73 (Fig. 9b). In contrast with amphibole, both the SPO and CPO strength of clinopyroxene appear to be also largely insensitive to grain size and aspect ratio (Fig. 9c).

The misorientation angle distribution of clinopyroxene in all samples does not significantly differ from the theoretical random distribution (i.e., the "uniform" green curve; Fig. 10b), except in the monomineralic layer A1 in sample SE13-67. Small

misorientation angles (from 2 to 10°) largely prevail. They correspond to rotations essentially around the [010] and the [001] axis (Fig. 10c), which corresponds to the mechanical twinning axis, as previously reported for clinopyroxene deformed at high temperature conditions (Frets 2012).

5.4.3 Plagioclase

Plagioclase has a weak CPO (Fig. 11a, S5c-d). Its strength is similar to that of clinopyroxene, with a J-index varying between 1.51 and 2.06 (Fig. 9a). Plagioclase grains display a concentration of (001) poles normal to the foliation plane and [100] axes subparallel to the lineation (Fig. 11a). Poles to (010) show no preferred alignment. The CPO strength and patterns do not vary with the distance from the contact, nor with the mineral assemblage.

The misorientation angle distribution of plagioclase in all samples slightly differs from the theoretical random distribution (i.e., the "uniform" green curve; Fig. 11b). Small misorientation angles (from 2 to 10°) are largely dominant. They correspond to rotations around the twinning axis [100], and to a much lesser extent around the [001] axis (Fig. 11c). However, the [001] axis becomes the main axis of intracrystalline misorientations in sample (SE13-76), where plagioclase is the load-bearing phase (Fig. 11a).

6 Discussion

6.1 Deformation processes in amphibole

Amphibole in the amphibolites of the HT metamorphic sole has a very strong CPO (J-index ~ 5; Fig. 9), similar in orientation to what is commonly reported for strained amphibole (Berger and Stünitz, 1996; Cao et al., 2010; Díaz Aspiroz et al., 2007; Elyaszadeh et al., 2018; Getsinger et al., 2013; Gomez Barreiro et al., 2010; Hacker and Christie, 1990; Imon et al., 2004; Tatham et al., 2008). This strong CPO is consistent with the extreme tectonic thinning and large shear strain of the HT metamorphic soles ($\gamma \geq 5$; Soret et al., 2017). For amphibole with J-index of ~3 and ~5, shear strains of ≥ 5 and ≥ 10 have been reported in amphibolite in deformation experiments (Getsinger, 2015) and in continental shear zones (Tatham et al., 2008), respectively (Fig. 9a). However, as for amphibole in the Semail HT metamorphic sole, those amphibole crystals show no or little evidence for intracrystalline plastic deformation and coexisting phases (plagioclase, clinopyroxene and quartz) have a weak CPO. In the light of our observations (see also Table 2) we discuss below possible deformation mechanisms and their relative contributions:

6.1.1 Dislocation creep

If the strong amphibole CPO and the observed subgrain misorientations (Fig. 7) result from intracrystalline plastic deformation, the misorientation axis should be perpendicular to the direction of crystal slip (e.g., Lloyd et al., 1997). In our study, however, intracrystalline misorientations are essentially accommodated around the [001] axis, and only to a lesser extent around the

[010] axis (Fig. 7b). Most of the misorientations are therefore incompatible with the activation of the amphibole easy slip system (100)[001], that would account for the observed CPO geometries and subgrain misorientations (Fig. 7a). Moreover, because the rotation axis of misoriented domains in amphibole grains is parallel to the lineation, they do not record large shear strain, assuming intracrystalline plasticity as the dominant deformation mechanism. Conversely, the [010] rotation axis (Fig. 7b), lying in the foliation plane perpendicularly to the general shear sense, is compatible with the activation of the amphibole easy slip system. The relatively small amount of rotation axes oriented parallel to [010] is also consistent with the fact that only few of the Ti-rich amphibole grains recording peak T conditions (~850°C) show microstructural evidence for plastic deformation (such as subgrain formation; SE13-67; Fig. 8a-c). The larger amount of [010] rotation axes in amphibole in the more retrogressed samples (SE13-69, SE13-76; Fig. 7c) correlates with an increasing microstructural evidence for dynamic recrystallization of amphibole in these rocks. This suggests that Ti-low amphibole (unlike higher T amphibole) may have accommodated part of the shear strain in the dislocation creep regime, especially in rocks more pervasively re-equilibrated at lower temperatures (~750°C; SE13-76).

6.1.2 Grain boundary sliding

The strong correlation between the aspect ratio, the CPO and SPO intensities, and the alignment of the long axes subparallel to the [001] crystallographic axis (Fig. 8) outline the tight relationship between grain shape, grain size and shape orientation of amphibole (Figs. 9c, S1). The general high fab ength of amphibole in all samples (Figs. 7-9, S1) therefore advocates for a component of rigid grain rotation driven by grain boundary sliding in the strain accommodation from peak to retrograde conditions (as previously reported in other settings; Berger and Stünitz 1996; Díaz Azpiroz et al. 2007; Elyaszadeh et al., 2018; Ildefonse et al. 1990; Shelley 1994; Tatham et al. 2008).

6.1.3 Dissolution-precipitation creep

In all samples amphibole grains commonly show lobate grain boundaries, and in the more retrogressed samples (SE13-69, SE13-76) they display small and patchy Ti-high cores truncated by the crystallization of secondary Ti-medium to Ti-low amphibole, especially along micro-fractures (Fig. 6k-m). These observations point to dissolution with the precipitation of secondary amphibole and other phases such as plagioclase and ilmenite (Figs. 6j-m). Fluid-driven mineral reactions and heterogeneous nucleation in the garnet-clinopyroxene amphibolite were pervasive and continuous during cooling is also supported by the presence of amphibole and plagioclase in healed micro-fractures of clinopyroxene porphyroclasts, at grain boundaries of dynamically recrystallized clinopyroxene, and more generally in the matrix at the expense of garnet and clinopyroxene.

As for Ti-rich amphibole grains crystallized at peak conditions, secondary amphibole grains have a strong SPO/CPO, characterized by the [001] axis (i.e., the long axis) parallel to the lineation (Figs. 6h,i,l,m, 8c). Pervasive precipitation of

secondary amphibole with a SPO/CPO parallel to the lineation indicates extensive and continuous oriented solution transfer during cooling of the garnet-clinopyroxene amphibolite unit (e.g., Berger and Stünitz, 1996; Shelley, 1994).

6.1.4 Brittle deformation

The high micro-fracture densities in coarse amphibole grains (Figs. 5a, 6a-b) and the general fine-grained size in the best preserved sample (SE13-67) attest to grain size reduction through brittle deformation starting at or after peak conditions. This brittle behaviour of amphibole within a rock deforming ductilely at high temperature has already been reported (Berger and Stunitz, 1996; Diaz Aspiroz et al., 2007; Giuntoli et al., 2018; Gomez Barreiro et al., 2010, Imon et al., 2002; Ko and Jung, 2015; Nyman et al, 1992) but ascribed to significantly lower deformation temperatures (≤ 700˚C). Preferential micro-fracturing along planes including the long ([001]) crystallographic axis could explain the similar aspect ratios of fine and coarse amphibole grains (essentially ≤ 2–3, as suggested by Gomez Barreiro et al. (2010). Micro-fracturing along the [001] crystallographic axis together with small rigid rotations (1–3°; Fig. 6e-h) may further explain some of the apparent intracrystalline misorientations in amphibole around the [001] rotation axis (Figs. 6j, 7c)

Brittle deformation at or near peak conditions is also supported by the presence of garnet grains exhibiting fractures filled by the polyphase matrix and of the healed, fluid-filled micro-fractures in clinopyroxene porphyroclasts. Some, but less common, micro-fracturing is also observed in secondary amphibole crystals grown during retrograde P–T conditions (in SE13-69 and SE13-76), indicating that brittle deformation persisted during cooling. This is further supported by the ubiquitous presence of wider epidote- and prehnite-filled fractures crosscutting the entire HT amphibolite (Fig. 2d).

These brittle deformation events could have resulted from i) mechanical interactions between coarse and elongate amphibole grains hampering rigid particle rotation (i.e., true collisions or disturbance of the flow in the matrix due to neighbouring phases; Ildefonse et al., 1992) and/or ii) fluid-driven embrittlement and transient changes in pore-fluid pressure during dehydration (and/or melting) at peak conditions (e.g., Brodie and Rutter, 1985) or during the onset of retrogression (i.e., fluid ingression from adjacent slab dehydration; e.g., in a colder subduction context: Locatelli et al., 2018).

The development of micro-fractures enhanced permeability, fluid circulation and retrograde hydration, thereby promoting further micro-fracturing but also dissolution-precipitation creep in the rock. Dissolution-precipitation creep was likely driven by the metastability of the peak assemblage during cooling and hydration. Such positive feedback between viscous and/or brittle deformation and (hydrous) mineral reactions was recently described in shear experiments on amphibolites conducted at 600–800°C and 0.5–1.5 GPa (Marti et al., 2017). By contrast, in rocks pervasively re-equilibrated at lower temperatures conditions in the amphibole–plagioclase stability field (~750°C; SE13-76), dissolution-precipitation creep was partly inhibited, and dislocation creep became more effective.

Solid Earth Discuss., https://doi.org/10.5194/se-2019-28
Manuscript under review for journal Solid Earth
Discussion started: 14 February 2019

6.2 Deformation processes in clinopyroxene

In sample SE13-67, clinopyroxene forms σ-type porphyroclasts and monomineralic fine-grained aggregates wrapped around by a matrix of Amp ± Cpx ± Pl (Fig. 2d-f). Similarly to garnet, clinopyroxene appears therefore to be mechanically stronger than the polyphase matrix.

In contrast to amphibole, clinopyroxene porphyroclasts show ubiquitous microstructural evidence for intracrystalline plasticity, such as undulose extinction and well-developed core-and-mantle structures (Fig. 5f-h) testifying to dynamic recrystallization by subgrain rotation (as interpreted by Bascou et al., 2002; Bystricky and Mackwell, 2001; Kenkmann and Dresen, 2002). Clinopyroxene has a CPO pattern characterized by the [001] axis maximum subparallel to the lineation (Figs. 8d-f, 10a), and girdle concentrations of both (100) and (010) poles perpendicular to the lineation (Figs. 10a). This pattern likely reflects the dominant activation of the {hk0}[001] glide systems in the dislocation creep regime, as commonly reported in experiments on omphacite and diopside (Bascou et al., 2002; Getsinger and Hirth, 2014; Ingrin et al., 1991). Associated intracrystalline misorientations are essentially accommodated around the [010] axis (Fig. 10c), especially in the fine-grained monomineralic aggregates. However, the CPO strength is low to moderate, with some dispersion of the [001] axis, even in the fine-grained monomineralic aggregates (Figs. 10a, S5b). The weakening of the CPO and the presence of randomly-oriented minute amphibole at the grain boundaries of recrystallized clinopyroxene testify to GBS activation syn- to post- grain size reduction by dynamic recrystallization, even in the mono-mineralic layers (A1; SE13-67).

It is noteworthy that some trails of secondary fluid inclusions representing healed fluid-filled micro-fractures in the core of clinopyroxene porphyroclasts (Fig. 5h) are slightly rotated and/or disappear within the newly recrystallized grains, confirming that some brittle deformation preceded dynamic recrystallization — therefore at or slightly after peak conditions.

6.3 Deformation processes in amphibolites

The highly deformed HT garnet-clinopyroxene amphibolites experienced grain size reduction (GSR), starting from or slightly after peak T conditions with extensive (and multiple) fluid-driven micro-fracturing events affecting amphibole, clinopyroxene and garnet (stage A1; Fig. 12a; Table 2). GSR was then promoted during early exhumation, cooling (~850–800°C) and hydration, by pervasive and heterogeneous nucleation of new fine-grained phases (i.e., secondary amphibole, plagioclase, epidote). The combination of these processes promoted dissolution-precipitation creep accommodated by grain boundary sliding (GBS) and associated phase mixing (e.g. Kruse and Stünitz, 1999; Marti et al., 2017) as the dominant deformation mechanism within the garnet-clinopyroxene amphibolite. Dissolution-precipitation creep and GBS inhibited further grain growth by pinning of secondary phases and likely induced significant strain softening during incipient retrogression and cooling (stage A2; Fig. 12a; ; Table 2).

Solid Earth Discuss., https://doi.org/10.5194/se-2019-28
Manuscript under review for journal Solid Earth
Discussion started: 14 February 2019

Clinopyroxene porphyroclasts, mechanically stronger than the fine-grained polymineralic matrix, accommodated early deformation in the dislocation creep regime. Dynamically recrystallized clinopyroxene has a lower Na-content, indicating that dislocation creep initiated after the onset of exhumation (Soret et al., 2017). The weaker CPO of clinopyroxene in polymineralic layers re y to monomineralic layers and the presence of interstitial minute amphibole in between recrystallized clinopyroxene grains indicate that the newly-formed clinopyroxene grains accommodated further deformation preferentially by dissolution-precipitation creep and grain boundary sliding. Contrary to amphibole, the low aspect ratio of clinopyroxene prevents preferential alignment parallel to the stretching direction during GBS. The p e of GBS postdating the dynamic recrystallization of clinopyroxene is also supported by the loss of microstructural nce for any competence contrast between phases known to have different strength in the retrogressed HTa amphibolite (sample SE13-69; Fig. 3a).

In rocks most affected by dissolution-precipitation, mineral reactions led to the predominance of newly formed minerals and to a drastic decrease of the number of phases. In this view, rock re-equilibration via the pervasive crystallisation of secondary amphibole and plagioclase, at the expense of metastable garnet, clinopyroxene and primary amphibole, may have inhibited further dissolution-precipitation and GBS, promoting growth of larger grains (stage B; Fig. 12a; Table 2). These secondary, coarser phases are also characterized by larger intracrystalline plastic deformation, indicating that dislocation creep became more efficient. The transition from GBS and dissolution-precipitation creep to dislocation creep thus probably occurred during hydration and cooling conditions, and probably relates to the grain size increase and greater thermodynamic stability of the new phases (stage B; Fig. 12a; Table 2).

6.4 Mechanical evolution of the plate interface during subduction infancy

During subduction infancy, the leading edge of the slab gets in contact with an increasingly strong, increasingly warmer and anhydrous mantle wedge acting as a buttress (Fig. 13a; Agard et al., 2016). Accretion of metamorphic soles to the basal peridotites of the future ophiolite reflects this increased mechanical coupling between the plates across a restricted P–T-time window (i.e., when viscosities of the slab crust and overlying mantle are similar; Agard et al., 2016). Our micro-structural data allow to document the evolution of the deformation at the top of the slab (stages A1-A2-B; Figs. 12, 13):

— Approximatively from amphibolite to granulite facies and up to 850 ± 50˚C – 1.0 GPa, the slab crust progressively dehydrates and minerals such as amphibole (Ti-medium/poor) and plagioclase are replaced by mechanically stronger garnet and clinopyroxene in the HTa unit (and Ti-rich amphibole; stage A1; Fig. 12a). The leading edge of the slab thus likely hardens (as shown by the evolution of the strength curve in figure 13). When it reaches the strength of the mantle on top, HTa gets stripped and becomes the first slice accreted to the upper plate peridotite (stage A; Fig. 13). Our observations suggest that a strong amphibole fabric dominates rock anisotropy at the top of the slab. This fabric is controlled by syn-kinematic oriented growth and rigid grain rotation, as shown by the strong correlation between grain size, aspect ratio and fabric intensity. The onset of brittle deformation in the garnet–clinopyroxene amphibolite leads to drastic grain size reduction (GSR; stage A1; Fig.

12a). This brittle deformation, possibly controlled by dehydration embrittlement (Davies, 1999), dehydration-driven stress transfer (Ferrand et al., 2017) and/or fluid ingression from adjacent slab dehydration may have acted as a precursor for strain localization in the garnet–clinopyroxene amphibolite within the downgoing slab (and therefore detachment of HTa; Fig. 13).

Similarly, fluids released at the plate interface during slab burial are thought to trigger early strain softening of the base of the mantle wedge through GSR promoted by fluid/mantle interaction and dissolution/precipitation processes (Fig. 13b; Prigent et al. 2018b; Soret et al., 2016). Overall, these coeval processes across the plate interface controlled the onset and location of strong mechanical coupling between the top of the slab and the base of the nascent mantle wedge (stage A; Fig. 13).

— from 850 down to 750°C and 1 to 0.7 GPa (stage A2 in Fig. 12a), early exhumation and cooling of the garnet–clinopyroxene bearing HTa is associated with strong shearing and pervasive retrogression across the plate interface (Soret et al., 2017; Prigent et al., 2018b). Deformation in HTa is extensively accommodated by dissolution-precipitation assisted by grain boundary sliding — including mineral reactions, heterogeneous nucleation and phase mixing — and to a lesser extent by dynamic recrystallization. The activation of dissolution-precipitation creep and GBS leads to significant strain softening of the exhuming HTa unit. Multiple brittle deformation events, observed from peak conditions to late exhumation (see sect. 6.3), may have contributed to facilitate fluid ingression and thereby enhanced mineral reactions and rock re-equilibration within HTa.

Syn-exhumation mechanical softening occurs also in the basal mantle wedge in the diffusion creep regime, as it becomes colder and more metasomatized (Fig. 13; Agard et al., 2016; Prigent et al., 2018a,b; Soret et al., 2016). Similar weakening on both sides of the plate interface maintains a coupling between HTa and the peridotites and explains their coeval early exhumation (from ~1 to 0.7 GPa).

— At temperatures around 750°C (stage B: Fig. 12b; Fig. 13), during later exhumation and cooling of HTa, pervasive fluid-rock interaction transforms the base of HTa into a two-phase matrix composed of syn-kinematic Ti-medium/low amphibole and plagioclase, with only minor amount of biotite and epidote. Meanwhile, the top of the subducting slab (i.e., the future plagioclase-rich HTb unit) consists of a similar mineral assemblage (Fig. 13). Our observations show that the dominant mode of viscous deformation in HTa progressively switches from dissolution–precipitation creep and GBS to dislocation creep, thus behaving potentially like the HTb unit. In the dislocation creep regime, the modal increase in plagioclase has a major softening effect. Mechanical coupling between HTb and HTa and/or HTb and the weakening at the base of the mantle wedge is responsible for the detachment and accretion of HTb (Fig. 13).

These deformation stages between 850 and 750°C result in the extreme thinning and distribution of similar HT metamorphic soles below the ophiolite (shear strain ≥5) and in the thinning of the base of the ophiolite itself (see discussion in Casey and Dewey, 2013).

6.5 Mechanical implications for warm subduction zones and oceanic/continental crustal-scale shear zones

Since pressure is not expected to significantly influence deformation mechanisms in the ductile regime, the viscosity at the top of the slab, and therefore the observed coupling with the overlying peridotites in mature warm subduction zones (at temperatures ≥ 800°C; e.g., Nankai, Cascapedia; Abers et al., 2017) may be controlled, as for HTa metamorphic soles, by the extent of fluid-rock interactions and the degree of stability of high-pressure amphibole.

Dissolution-precipitation creep and associated amphibole-forming reactions may also control strain localization, and therefore the development of long-lived oceanic detachments and core complexes in slow-spreading environments (Boschi et al., 2006; Escartin et al., 2003; Gülcher et al., 2019), as well as continental crustal-scale shear zones in collisional settings under cooling conditions and exhumation (Getsinger et al., 2013; Giuntoli et al., 2018; Tatham et al., 2008).

Finally, while many different interpretations have been invoked for the deformation mechanisms of amphibole and amphibolites (e.g., GBS, diffusion creep, dislocation creep; see sect. 2), such diversity could reflect change in P-T conditions, water activity and mineral stability. This study outlines that ongoing metamorphic processes and amphibole stability should be carefully taken into account when interpreting deformation mechanisms in amphibole, especially in shear zones experiencing hydration and cooling during exhumation, as a well-developed CPO in amphibole does not systematically testify to dislocation creep, and does not exclude a component of GBS in sheared amphibolites.

7 Conclusions

Based on micro-structural analysis and mineral chemistry, this study highlights the mineral-scale mechanisms controlling the progressive deformation of sheared amphibolites from the Oman metamorphic sole during subduction infancy, and unravels how strain is localized and accommodated in (hydrated) mafic rocks under amphibolite and granulite facies conditions. Metamorphic reactions and pore-fluid pressures driven by changes in P–T conditions and/or water activity are key controls on the rheology of mafic rocks and on the transition between brittle and viscous deformations at high temperature (as noted experimentally: Marti et al., 2017).

In high-temperature water-undersaturated conditions (850 ± 50°C), amphibole and amphibolites accommodate large shear strain essentially through cyclic grain boundary sliding, fracturing and grain size reduction. Amphibole is confirmed as one of the strongest minerals with little ability to deform in the dislocation creep regime. Fracturing occurs preferentially in monomineralic or polyphase aggregates (comprising also-strong, poorly oriented minerals such as garnet and clinopyroxene) where rigid grain rotation is inhibited.

In hydrated conditions at lower temperature (750±50°C), amphibole and amphibolite appear mechanically much weaker and tend to deform in the dislocation creep regime. Grain size reduction is mainly controlled by dynamic recrystallization, and grain boundary sliding is facilitated, especially in viscous polyphasic aggregates (e.g., comprising weak hydrous plagioclase).

In metastable and hydrated conditions (i.e., due to cooling and hydration on the return path), dissolution-precipitation caused by pervasive mineral reactions is the dominant deformation mechanisms in amphibole and mylonitic amphibolite. Dramatic grain size reduction and heterogeneous nucleation within the polyphase amphibolite enable GBS and phase mixing, thereby producing a large mechanical weakening. However, the fabric intensity of amphibole is not significantly affected by activation of GBS (contrary to the other phases) due to its specific high aspect ratio.

These mechanical evolutions, marked by strain hardening during increasing P–T conditions and by large strain softening during cooling, are respectively coeval with the detachment and early exhumation of the different amphibolitic units of the HT metamorphic sole. They probably control the extent of mechanical coupling between the top of the slab and the peridotites across the plate interface during subduction infancy (Agard et al., 2016; Prigent et al., 2018b).

As amphibole is commonly found with plagioclase, clinopyroxene and/or garnet in high-temperature shear zones, our pressure-independent findings may be applied to other geodynamic environments where similar temperatures, lithologies, fluid circulation and mechanical coupling between mafic rocks and peridotites prevail, such as in warm subduction zones (e.g., Nankai, Cascadia), in lower continental crust shear zones and oceanic detachments.

Author contributions

MS, PA and BD conceived the initial idea of the study. MS, PA, BD and CP participated in the fieldwork. MS conducted EBSD and EMP analyses. MS and BI performed EBSD data processing using MTEX. MS prepared the manuscript with contributions from all co-authors.

Competing interests

The authors declare no competing interests.

Acknowledgment

We thank F. Barou (Univ. Montpellier, France) for technical support on EBSD, N. Rividi, M. Fialin (CAMPARIS, Sorbonne Univ., Paris, France) and I. Di Carlo (Univ. Orléans, France) for technical support on EMP, C. Nevado and D. Delmas (Univ. Montpellier) for the polishing of thin-sections, and M. Herwegh, L. Labrousse, E. Gnos, P. Yamato and R. Graziani for helpful discussions. This work was essentially funded through the ONLAP project (ANR blanche, SIMI6; 2010 BLAN 615 01). Additional support was provided by an IUF grant (Institut universitaire de France) to PA.

References

Abers, G. A., Van Keken, P. E., and Hacker, B. R. The cold and relatively dry nature of mantle forearcs in subduction zones. Nat. Geosci., 5, 333–337. doi:10.1038/ngeo2922. 2017.

Agard, P., Yamato, P., Soret, M., Prigent, C., Guillot, S., Plunder, A., Chauvet, A., and Monié, P. Plate interface rheological switches during subduction infancy: control on slab penetration and metamorphic sole formation. Earth Planet. Sc. Lett., 451, 208–220. doi:10.1016/j.epsl.2016.06.054. 2016.

Agard, P., Plunder, A., Angiboust, S., Bonnet, G., and Ruh, J. The subduction plate interface: Rock record and mechanical coupling (from long to short time scales). Lithos. doi.org:10.1016/j.lithos.2018.09.029. 2018.

Ambrose, T. K., Wallis, D., Hansen, L. N., Waters, D. J., and Searle, M. P. Controls on the rheological properties of peridotite at a palaeosubduction interface: A transect across the base of the Oman–UAE ophiolite. Earth Planet. Sc. Lett., 491, 193–206. doi.org/10.1016/j.epsl.2018.03.027. 2018.

Bachmann, F., Hielscher, R., and Schaeben, H. Texture Analysis with MTEX – Free and Open Source Software Toolbox. Sol. St. Phen., 160, 63–68. doi:10.4028/www.scientific.net/SSP.160.63. 2010.

Bascou, J., Tommasi, A., and Mainprice, D. Plastic deformation and development of clinopyroxene lattice preferred orientations in eclogites. J. Struct. Geology, 24, 1357–1368. doi:10.1016/S0191-8141(01)00137-7. 2002.

Berger, A., and Stünitz, H. Deformation mechanisms and reaction of hornblende: examples from the Bergell tonalite (Central Alps). Tectonophysics, 257, 149–174. doi:10.1016/0040-1951(95)00125-5. 1996.

Boschi, C., Früh-Green, G. L., Delacour, A., Karson, J. A., and Kelley, D. S. Mass transfer and fluid flow during detachment faulting and development of an oceanic core complex, Atlantis Massif (MAR 30°N). Geochem. Geophy. Geosy., 7, Q01004. doi:10.1029/2005GC001074. 2006.

Boudier, F., Ceuleneer, G., and Nicolas, A. Shear zones, thrusts and related magmatism in the Oman ophiolite: Initiation of thrusting on an oceanic ridge. Tectonophysics, 151, 275–296. doi:10.1016/0040-1951(88)90249-1. 1988.

Brodie, K. H. Variation in amphibole and plagioclase composition with deformation. Tectonophysics, 78, 385–402. doi:10.1016/0040-1951(81)90021-4. 1981.

Brodie, K. H., and Rutter, E. H. On the relationship between rock deformation and metamorphism with special reference to the behaviour of basic rocks. Metamorphic Reactions, 4, 138–179. doi:10.1007/978-1-4612-5066-1_6. 1985.

Bunge, H. J. Texture Analysis in Materials Science, Butterworth's, London, 351–401. 1982.

Bystricky, M., and Mackwell, S. Creep of dry clinopyroxene aggregates. J. Geophy. Res., 106, 13443. doi:10.1029/2001JB000333. 2001.

Cao, S., Liu, J., and Leiss, B. Orientation-related deformation mechanisms of naturally deformed amphibole in amphibolite mylonites from the Diancang Shan, SW Yunnan, China. J. Struct. Geology, 32, 606–622. doi:10.1016/j.jsg.2010.03.012. 2010.

Davies, H. L. The role of hydraulic fractures and intermediate-depth earthquakes in generating subduction-zone magmatism. Nature, 328, 142–145. doi:10.1038/18202. 1999.

Dewey, J. F., and Casey, J. F. The sole of an ophiolite: the Ordovician Bay of Islands Complex, Newfoundland. J. Geol. Soc. London, 170, 715–722. doi:10.1144/jgs2013-017. 2013.

Díaz Aspiroz, M., Lloyd, G. E., and Fernández, C. Development of lattice preferred orientation in clinoamphiboles deformed under low-pressure metamorphic conditions. A SEM/EBSD study of metabasites from the Aracena metamorphic belt (SW Spain). J. Struct. Geology, 29, 629–645. doi:10.1016/j.jsg.2006.10.010. 2007

Dimanov, A., Rybacki, E., Wirth, R., and Dresen, G. Creep and strain-dependent microstructures of synthetic anorthite-diopside aggregates. J. Struct. Geology, 29, 1049–1069. doi:10.1016/j.jsg.2007.02.010. 2007.

Elyaszadeh, R., Prior, D. J., Sarkarinejad, K., and Mansouri, H. Different slip systems controlling crystallographic preferred orientation and intracrystalline deformation of amphibole in mylonites from the Neyriz mantle diapir, Iran. J. Struct. Geology, 107, 38-52. doi: 10.1016/j.jsg.2017.11.020. 2018

Ernst, W., and Liu, J. Experimental phase-equilibrium study of Al-and Ti-contents of calcic amphibole in MORB - A semiquantitative thermobarometer. Am. Mineral., 83, 952–969. doi: 10.2138/am-1998-9-1004. 1998.

Escartín, J., Mével, C., MacLeod, C. J., and McCaig, A. M. Constraints on deformation conditions and the origin of oceanic detachments: The Mid-Atlantic Ridge core complex at 15 45 N. Geochem. Geophy. Geosy., 4. doi:10.1029/2002GC000472. 2003.

Ferrand, T. P., Hilairet, N., Incel, S., Deldicque, D., Labrousse, L., Gasc, J., … Schubnel, A. Dehydration-driven stress transfer triggers intermediate-depth earthquakes. Nat. Commun., 8, 1–11. doi.org/10.1038/ncomms15247. 2017.

Getsinger, A. J. The Rheology of Amphibolite. Brown University. Ph.D. Thesis. 2015.

Getsinger, A. J., Hirth, G., Stünitz, H., and Goergen, E. T. Influence of water on rheology and strain localization in the lower continental crust. Geochem. Geophy. Geosy., 14, 2247–2264. doi:10.1002/ggge.20148. 2013.

Getsinger, A. J., and Hirth, G. Amphibole fabric formation during diffusion creep and the rheology of shear zones. Geology, 42, 535–538. doi:10.1130/G35327.1. 2014.

Giuntoli, F., Menegon, L., and Warren, C. J. Replacement reactions and deformation by dissolution and precipitation processes in amphibolites. J. Metamorph. Geol. doi.org/10.1111/jmg.12445. 2018.

Gnos, E. Peak Metamorphic Conditions of Garnet Amphibolites Beneath the Semail Ophiolite: Implications for an Inverted Pressure Gradient. Int. Geol. Rev., 40, 281–304. doi:10.1080/00206819809465210. 1998.

Gómez Barreiro, J., Martínez Catalán, J. R., Prior, D., Wenk, H. -R., Vogel, S., Díaz García, F., Arenas, R., Sanchez Martinez, S., and Lonardelli, I. Fabric Development in a Middle Devonian Intraoceanic Subduction Regime: The Careón Ophiolite (Northwest Spain). J. Geol., 118, 163–186. doi.org/10.1086/649816. 2010.

Gray, D. R., and Gregory, R. T. Implications of the structure of the Wadi Tayin metamorphic sole, the Ibra-Dasir block of the Samail ophiolite, and the Saih Hatat window for late stage extensional ophiolite emplacement, Oman. Mar. Geophy. Res., 21, 211–227. doi:10.1023/A:1026772717865. 2000.

Guilmette, C., Smit, M. A., Hinsbergen, D. J. J. Van, Gürer, D., Corfu, F., Charette, B., … Savard, D. Forced subduction initiation recorded in the sole and crust of the Semail Ophiolite of Oman. Nat. Geosci. doi:10.1038/s41561-018-0209-2. 2018.

Gülcher, A. J. P., Beaussier, S. J., and Gerya, T. V. On the formation of oceanic detachment faults and their influence on intra-oceanic subduction initiation: 3D thermomechanical modeling. Earth Planet. Sc. Lett., 506, 195–208. doi:10.1016/j.epsl.2018.10.042. 2019.

Hacker, B. R. Simulation of the metamorphic and deformational history of the metamorphic sole of the Oman ophiolite. J. Geophy. Res.-Solid Earth, 95, 4895–4907. doi:10.1029/JB095iB04p04895. 1990.

Hacker, B. R., and Christie, J. M. Brittle/Ductile and Plastic/Cataclastic Transitions in Experimentally Deformed and Metamorphosed Amphibolite. Geoph. Monog. Series., 56, 127–148. doi:10.1029/GM056p0127. 1990.

Hielscher, R., and Schaeben, H. A novel pole figure inversion method: Specification of the MTEX algorithm. J. Appl. Crystallography, 41, 1024–1037. doi:10.1107/S0021889808030112. 2008

Hier-Majumder, S., Mei, S., and Kohlstedt, D. L. Water weakening of clinopyroxenite in diffusion creep. J. Geophy. Res.-Sol. Ea., 110, 1–12. doi:10.1029/2004JB003414. 2005.

Ildefonse, B., Lardeaux, J. M., and Caron, J. M. The behavior of shape preferred orientations in metamorphic rocks: amphiboles and jadeites from the Monte Mucrone area (Sesia-Lanzo zone, Italian Western Alps). J. Struct. Geology, 12, 1005–1011. doi:10.1016/0191-8141(90)90096-H. 1990.

Ildefonse, B., Sokoutis, D., and Mancktelow, N. S. Mechanical interactions between rigid particles in a deforming ductile matrix. Analogue experiments in simple shear flow. J. Struct. Geology, 14, 1253–1266. doi:10.1016/0191-8141(92)90074-7. 1992.

Imon, R., Okudaira, T., and Kanagawa, K. Development of shape- and lattice-preferred orientations of amphibole grains during initial cataclastic deformation and subsequent deformation by dissolution-precipitation creep in amphibolites from the Ryoke metamorphic belt, SW Japan. J. Struct. Geology, 26(5), 793–805. doi:10.1016/j.jsg.2003.09.004. 2004.

Ingrin, J., Doukhan, N., and Doukhan, J. C. High-Temperature Deformation of Diopside Single-Crystal .2. Transmission Electron-Microscopy Investigation Of The Defect Microstructures. J. Geophy. Res.-Solid Earth And Planets, 96, 14287–14297. doi:10.1029/91JB01233. 1991.

Ji, S., Shao, T., Michibayashi, K., Long, C., Wang, Q., Kondo, Y., Zhao, W., Wang, H., and Salisbury, M. H. A new calibration of seismic velocities, anisotropy, fabrics, and elastic moduli of amphibole-rich rocks. J. Geophy. Res.-Sol. Ea., 118, 4699-4728. doi: 10.1002/jgrb.50352. 2013.

Kenkmann, T., and Dresen, G. Dislocation microstructure and phase distribution in a lower crustal shear zone - An example from the Ivrea-Zone, Italy. Int. J. Earth Sci., 91, 445–458. doi:10.1007/s00531-001-0236-9. 2002.

Kim, D., Katayama, I., Wallis, S., Michibayashi, K., Miyake, A., Seto, Y., and Azuma, S. Deformation microstructures of glaucophane and lawsonite in experimentally deformed blueschists: Implications for intermediate-depth intraplate earthquakes. J. Geophy. Res.-Sol. Ea., 120, 1229–1242. doi:10.1002/2014JB011528. 2015.

Ko, B., and Jung, H. Crystal preferred orientation of an amphibole experimentally deformed by simple shear. Nat. Commun., 6, 6586. doi:10.1038/ncomms7586. 2015.

Kruse, R., and Stünitz, H. Deformation mechanisms and phase distribution in mafic high-temperature mylonites from the Jotun Nappe, southern Norway. Tectonophysics, 303, 223–249. 1999.

Locatelli, M., Verlaguet, A., Agard, P., Federico, L., and Angiboust, S. Intermediate-depth brecciation along the subduction plate interface (Monviso eclogite, W. Alps). Lithos, doi:10.1016/j.lithos.2018.09.028. 2018.

Lloyd, G. E., Farmer, A. B., and Mainprice, D. Misorientation analysis and the formation and orientation of subgrain and grain boundaries. Tectonophysics, 279, 55–78. doi:10.1016/S0040-1951(97)00115-7. 1997.

Lloyd, G. E., Butler, R. W. H., Casey, M., Tatham, D. J., and Mainprice, D. Constraints on the seismic properties of the middle and lower continental crust. Geol. Soc. Spec. Publ., 360, 7–32. doi:10.1144/SP360.2. 2011.

Mainprice, D., and Nicolas, A. Development of shape and lattice preferred orientations: application to the seismic anisotropy of the lower crust. J. Struct. Geology, 11, 175–189. doi:10.1016/0191-8141(89)90042-4. 1989.

Mainprice, D., Bachmann, F., Hielscher, R., Schaeben, H. Descriptive tools for the analysis of texture projects with large datasets using MTEX: strength, symmetry and components. Geol. Soc. Spec. Publ., 409, 251–271. doi:10.1144/SP409.8. 2014.

Marti, S., Stünitz, H., Heilbronner, R., Plümper, O., and Drury, M. Experimental investigation of the brittle-viscous transition in mafic rocks – Interplay between fracturing, reaction, and viscous deformation. J. Struct. Geology, 105, 62–79. doi:10.1016/j.jsg.2017.10.011. 2017.

Nicolas, A., Boudier, F., Ildefonse, B., and Ball, E. Accretion of Oman and United Arab Emirates ophiolite – Discussion of a new structural map. Mar. Geophy. Res., 21, 147–179. doi:10.1023/A:1026769727917. 2000.

Nyman, M. W., Law, R. D., and Smelik, E. A. Cataclastic deformation for the development of core mantle structures in amphibole. Geology, 20, 455–458. doi:10.1130/0091-7613(1992)020<0455. 1992.

Plunder, A., Agard, P., Chopin, C., Soret, M., Okay, A. I., and Whitechurch, H. Metamorphic sole formation, emplacement and blueschist facies overprint: early subduction dynamics witnessed by western Turkey ophiolites. Terra Nova, 28(5), 329–339. doi.org:10.1111/ter.12225. 2016.

Prigent, C., Guillot, S., Agard, P., Lemarchand, D., Soret, M., and Ulrich, M. Transfer of subduction fluids into the deforming mantle wedge during nascent subduction: Evidence from trace elements and boron isotopes (Semail ophiolite, Oman). Earth Planet. Sc. Lett., 484, 213–228. doi.org:10.1016/j.epsl.2017.12.008. 2018a.

Prigent, C., Guillot, S., Agard, P., and Ildefonse, B. Fluid-Assisted Deformation and Strain Localization in the Cooling Mantle Wedge of a Young Subduction Zone (Semail Ophiolite). J. Geophy. Res.-Sol. Ea., 1–21. doi.org:10.1029/2018JB015492. 2018b.

Prigent, C., Agard, P., Guillot, S., Godard, M. and Dubacq, B. Mantle wedge deformation during subduction infancy: evidence from the base of the Semail ophiolitic mantle, J. Petrol., egy090, doi:10.1093/petrology/egy090. 2018c.

Rioux, M., Garber, J., Bauer, A., Bowring, S., Searle, M., Kelemen, P., and Hacker, B. Synchronous formation of the metamorphic sole and igneous crust of the Semail ophiolite: New constraints on the tectonic evolution during ophiolite formation from high-precision U–Pb zircon geochronology. Earth Planet. Sc. Lett., 451, 185–195. doi:10.1016/j.epsl.2016.06.051. 2016.

Rybacki, E., and Dresen, G. Deformation mechanism maps for feldspar rocks. Tectonophysics, 382, 173–187. doi:10.1016/j.tecto.2004.01.006. 2004.

Schmidt, N.-H., and Olesen, N. Computer-aided determination of crystal-lattice orientation from electron-channeling patterns in the SEM. Can. Mineral., 27, 15–22. 1989.

Shelley, D. Spider texture and amphibole preferred orientations. J. Struct. Geology, 16, 709–717. doi:10.1016/0191-8141(94)90120-1. 1994.

Siegesmund, S., Helming, K., and Kruse, R. Complete texture analysis of a deformed amphibolite: comparison between neutron diffraction and U-stage data. J. Struct. Geology, 16, 131–142. doi:10.1016/0191-8141(94)90024-8. 1994.

Soret, M., Agard, P., Dubacq, B., Vitale-Brovarone, A., Monié, P., Chauvet, A., Whitechurch, H., Villemant, B. Strain localization and fluid infiltration in the mantle wedge during subduction initiation: Evidence from the base of the New Caledonia ophiolite. Lithos, 244, 1–19. doi:10.1016/j.lithos.2015.11.022. 2016.

Soret, M., Agard, P., Dubacq, B., Plunder, A., and Yamato, P. Petrological evidence for stepwise accretion of metamorphic soles during subduction infancy (Semail ophiolite, Oman and UAE). J. Metamorph. Geol., 35, 1050–1080. doi:10.1111/jmg.12267. 2017.

Tatham, D. J., Lloyd, G. E., Butler, R. W. H., and Casey, M. Amphibole and lower crustal seismic properties. Earth Planet. Sc. Lett., 267, 118–128. doi:10.1016/j.epsl.2007.11.042. 2008.

Wakabayashi, J., and Dilek, Y. Spatial and temporal relationships between ophiolites and their metamorphic soles: A test of models of forearc ophiolite genesis. Geol. Soc. Am. Spec. Publ., 349, 53–64. doi:10.1130/0-8137-2349-3.53. 2000.

Wakabayashi, J., and Dilek, Y. (2003). What constitutes “emplacement” of an ophiolite?: Mechanisms and relationship to subduction initiation and formation of metamorphic soles. Geol. Soc. Am. Spec. Publ., 218, 427–447. doi:10.1144/GSL.SP.2003.218.01.22. 2003.

Wenk, H. R., and Christie, J. M. Comments on the interpretation of deformation textures in rocks. J. Struct. Geology, 13, 1091–1110. doi:10.1016/0191-8141(91)90071-P. 1991.

Wheeler, J., Prior, D., Jiang, Z., Spiess, R., and Trimby, P. The petrological significance of misorientations between grains. Contrib. Mineral. Petr., 141, 109–124. doi:10.1007/s004100000225.

Solid Earth Discuss., https://doi.org/10.5194/se-2019-28
Manuscript under review for journal Solid Earth
Discussion started: 14 February 2019

Whitney, D. L., and Evans, B. W. Abbreviations for names of rock-forming minerals. Am. Min., 95, 185–187. doi:10.2138/am.2010.3371. 2010.

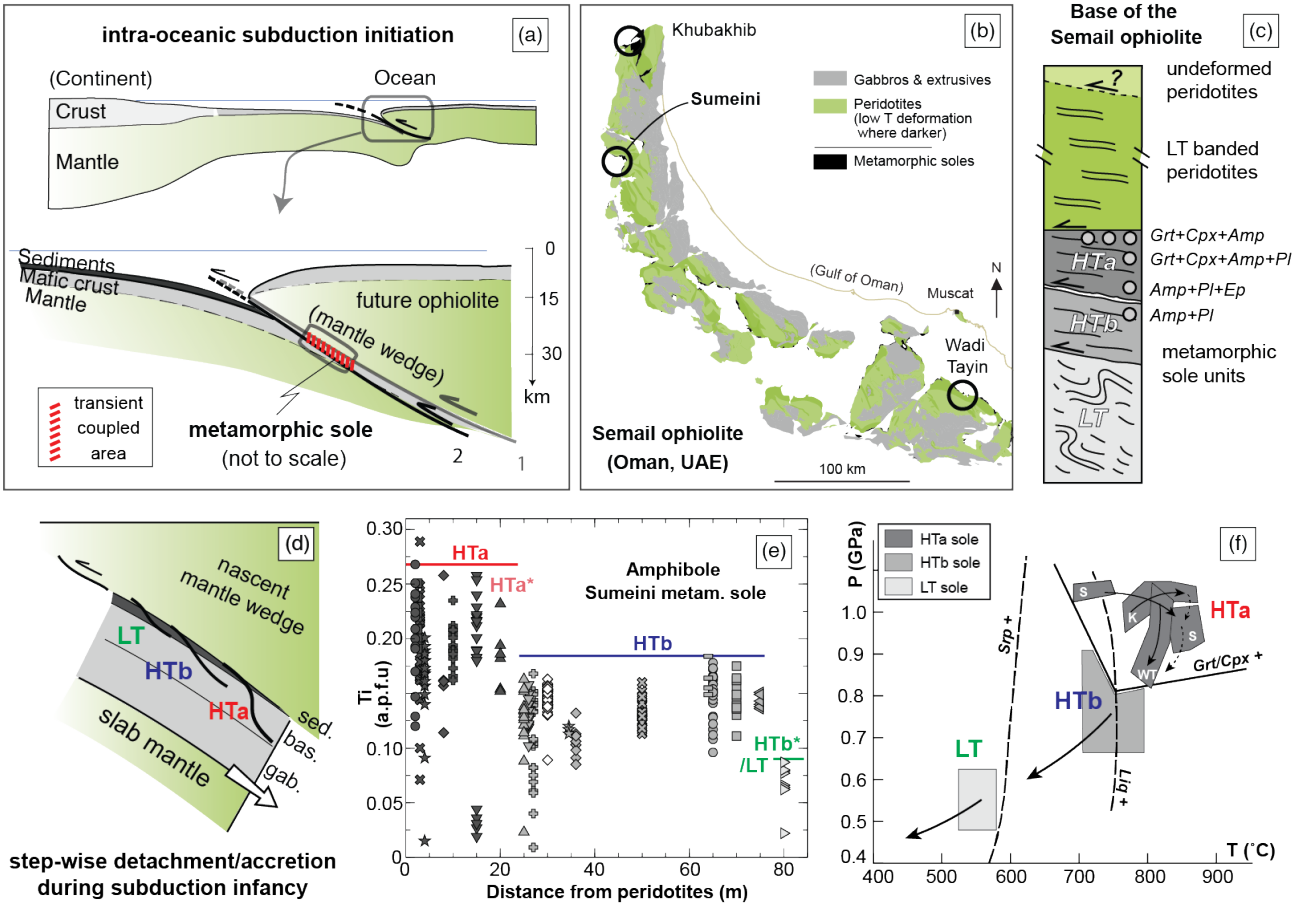

Figure 1: (a) Geodynamic setting of metamorphic sole formation during intra-oceanic subduction infancy; (b) Simplified geological map of the Semail ophiolite highlighting the outcrops of the metamorphic sole beneath the ophiolite mantle (modified after Nicolas et al., 2000); (c) schematic log of the base of the Oman ophiolite showing the structural position of the samples from Khubakhib (K), Sumeini (S) and Wadi Tayin (WT). See Table 1 for details; (g) Close-up view on the tectonic configuration along the nascent plate interface, during the formation and exhumation of the HTa, HTb and LT soles until reaching the steady state (sketch modified after Agard et al., 2016 and Soret et al., 2017). s: sediment, b: basalt, gabbro, m: mantle peridotite (e) Amphibole Ti vs. Si content in amphibole samples from Sumeini (after Soret et al., 2017) outlining the discontinuous decrease of T conditions during the exhumation of the HT metamorphic sole; (f) Compilations of P–T estimates and associated P–T paths (after Soret et al., 2017), from the Grt–Cpx amphibolite (HTa), to the Pl-rich amphibolite (HTb) and greenschist facies (LT) metamorphic sole units.

Solid Earth Discuss., https://doi.org/10.5194/se-2019-28
Manuscript under review for journal Solid Earth
Discussion started: 14 February 2019

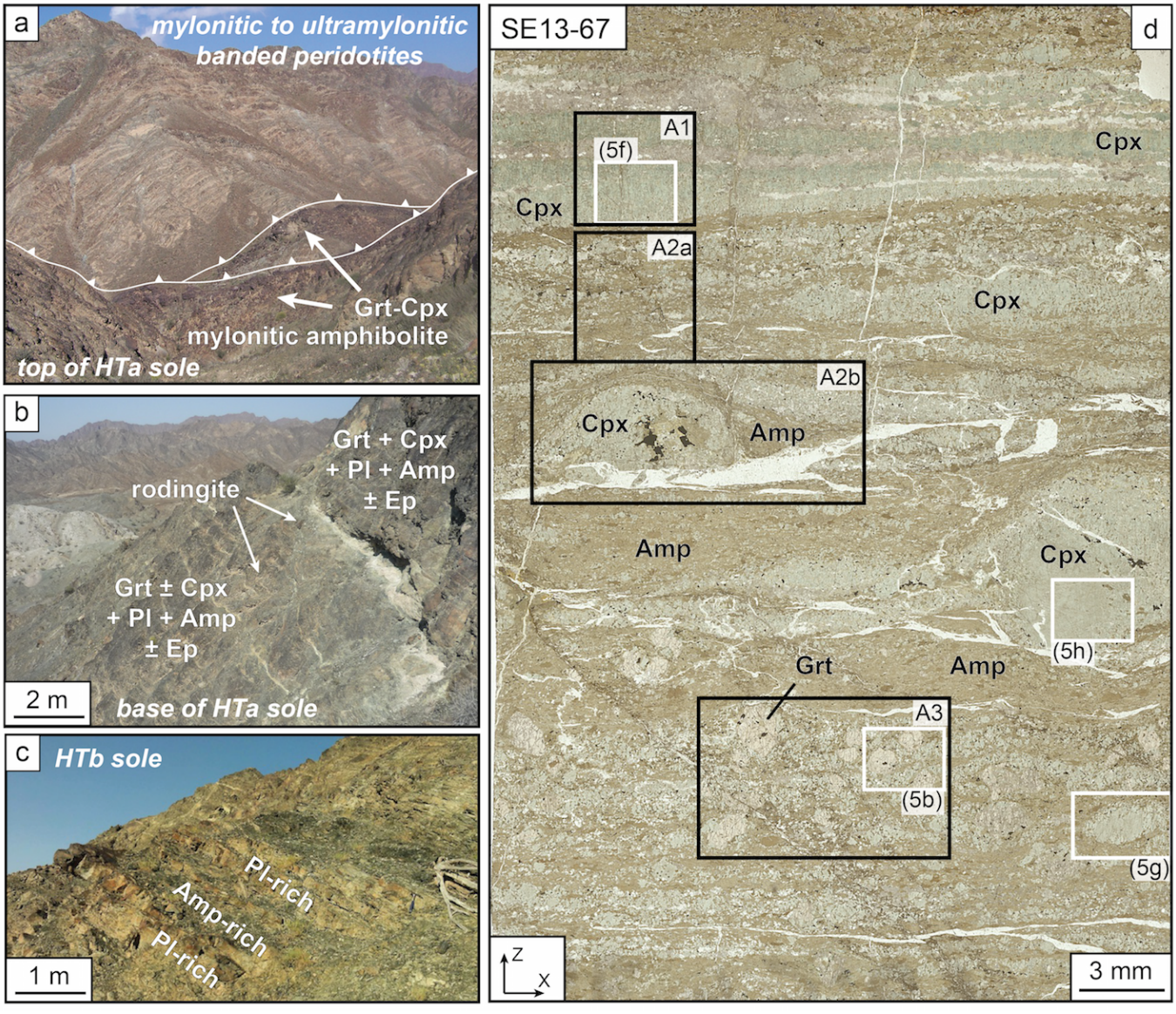

Figure 2: Photographs of the base of the Semail ophiolite outcropping in the Sumeini region. (a) Basal contact between banded peridotite and the Grt-Cpx amphibolite of the metamorphic sole (zone HTa); (b) base of the HTa unit, widely affected by Ca-rich metasomatism (rodintigization); (c) layered structure in zone HTb with alternations from plagioclase-rich to darker amphibole-rich layers; (d-h) Well-preserved mineral equilibrium texture and deformation structure from peak conditions in the HTa amphibolite at Sum~2.5 m from the contact). Black boxes refer to EBSD maps shown in Figs. 3 and 4. White boxes correspond to photog in Fig. 5.

Solid Earth Discuss., https://doi.org/10.5194/se-2019-28
Manuscript under review for journal Solid Earth
Discussion started: 14 February 2019

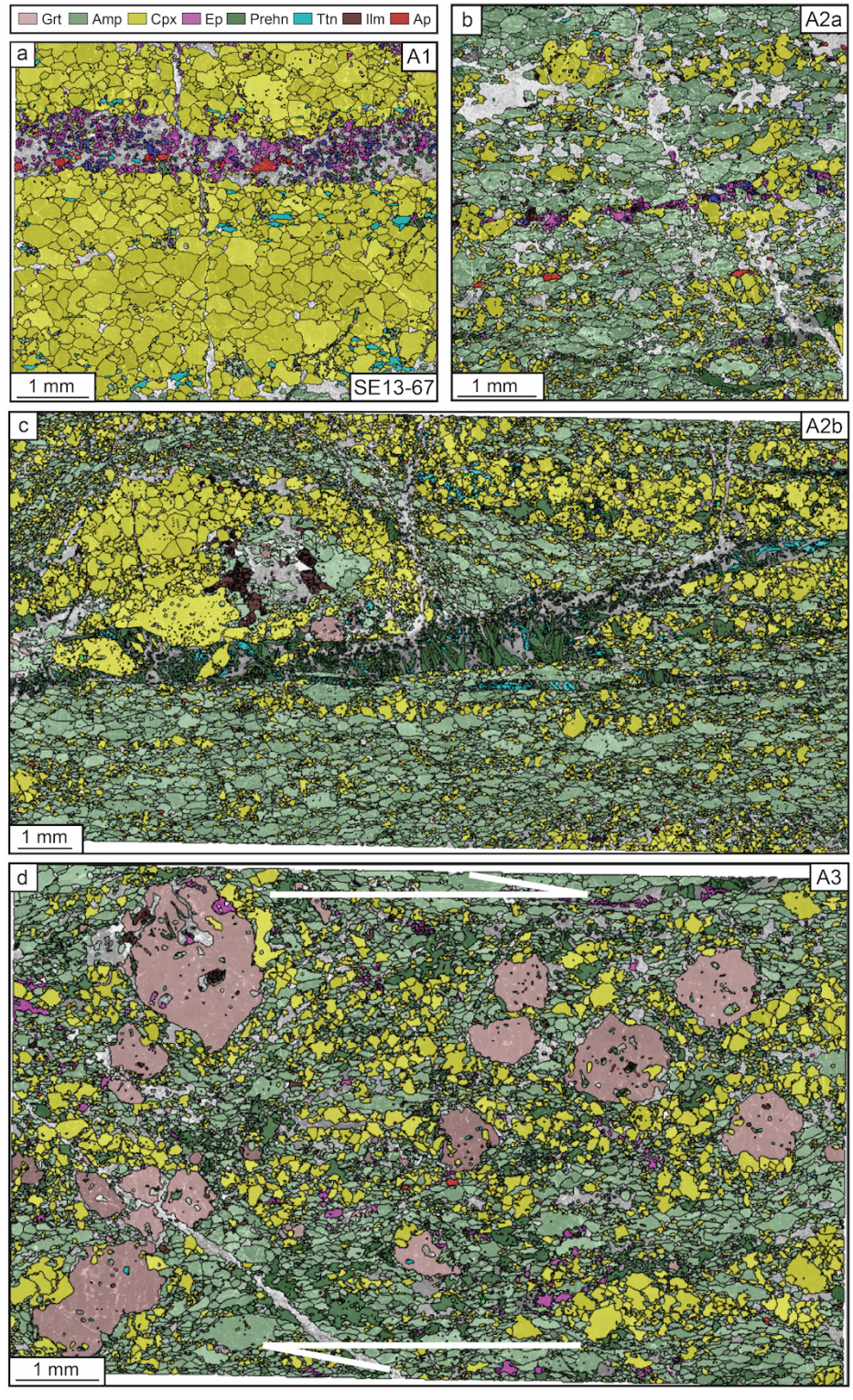

Solid Earth Discuss., https://doi.org/10.5194/se-2019-28
Manuscript under review for journal Solid Earth
Discussion started: 14 February 2019

Figure 3: EBSD phase maps from a Grt-Cpx–bearing amphibolite sampled at ~2.5m from the contact with peridotite (sample SE13-67) and showing the best-preserved micro-structures. (a) Area 1 (A1) composed essentially of clinopyroxene with a late vein of epidote; (b) and (c) Area 2 (A2) composed of amphibole and clinopyroxene. (c) A late prehnite vein crosscuts the sample; (d) Area 3 (A3) composed of garnet, amphibole and clinopyroxene.

5

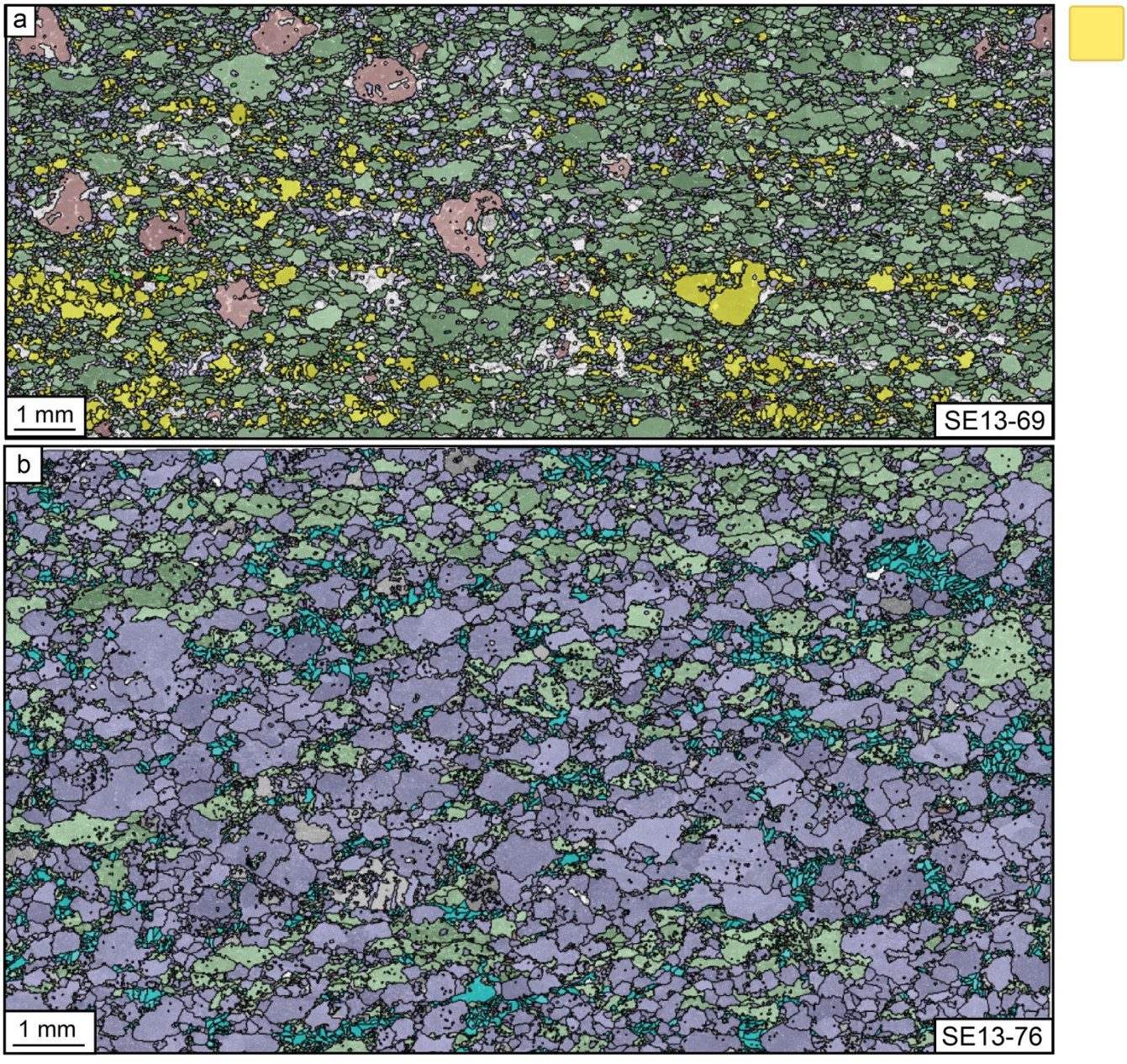

Figure 4: EBSD phase maps (a) from a slightly retrogressed at amphibolite facies garnet–clinopyroxene-bearing amphibolite at the top of HTa unit (sample SE13-69; Sumeini area), (b) from a highly retrogressed garnet-clinopyroxene-free amphibolite at the base of HTa unit (sample SE13-76; Sumeini area).

Solid Earth Discuss., https://doi.org/10.5194/se-2019-28
Manuscript under review for journal Solid Earth
Discussion started: 14 February 2019

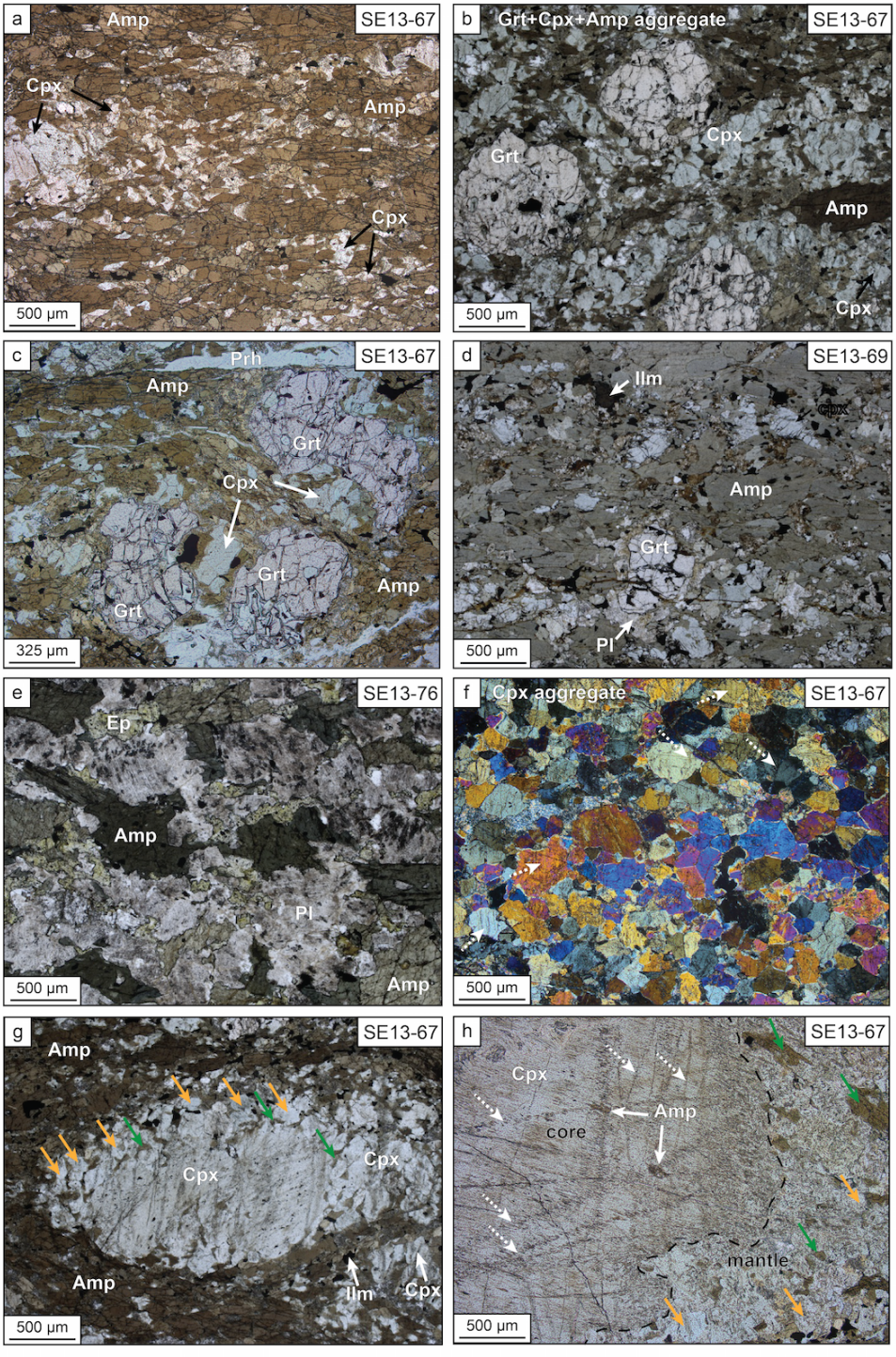

Solid Earth Discuss., https://doi.org/10.5194/se-2019-28
Manuscript under review for journal Solid Earth
Discussion started: 14 February 2019

Figure 5: Photographs of representative microstructures in the HTa amphibolites. (a) Cpx and amphibole well mixed in the amphibolitic matrix (A3; SE13-67). Amphibole showing high micro-fracture densities. (b) garnet porphyroclasts surrounded by a fine-grained matrix of Cpx+Amp (Area 3); (c) fractured garnet porphyroclast with fractures filled by a fine-grained matrix composed of Cpx+Amp; (d) ~8 m from the contact, showing greater retrogression characterized by an increase of plagioclase and brown amphibole at the expense of Grt+Cpx; (e) ~25 m from the contact (base of HTa), highly retrogressed amphibolite associated with secondary crystallization of fine grained brown to green amphibole, epidote and plagioclase; (f) monomineralic layer of recrystallized clinopyroxene by subgrain rotation; (g) sheared Cpx porphyroclast wrapped by fine grained brown Amp (Area 2); (h) Core-and-mantle structure in a Cpx porphyroclast with and minute amphibole in sealed micro-fractures (fluid inclusions trails) and at grain boundaries of the dynamic recrystallized mantle. Orange and green arrows point to dynamically recrystallized clinopyroxene and secondary amphibole, respectively. See details in text.

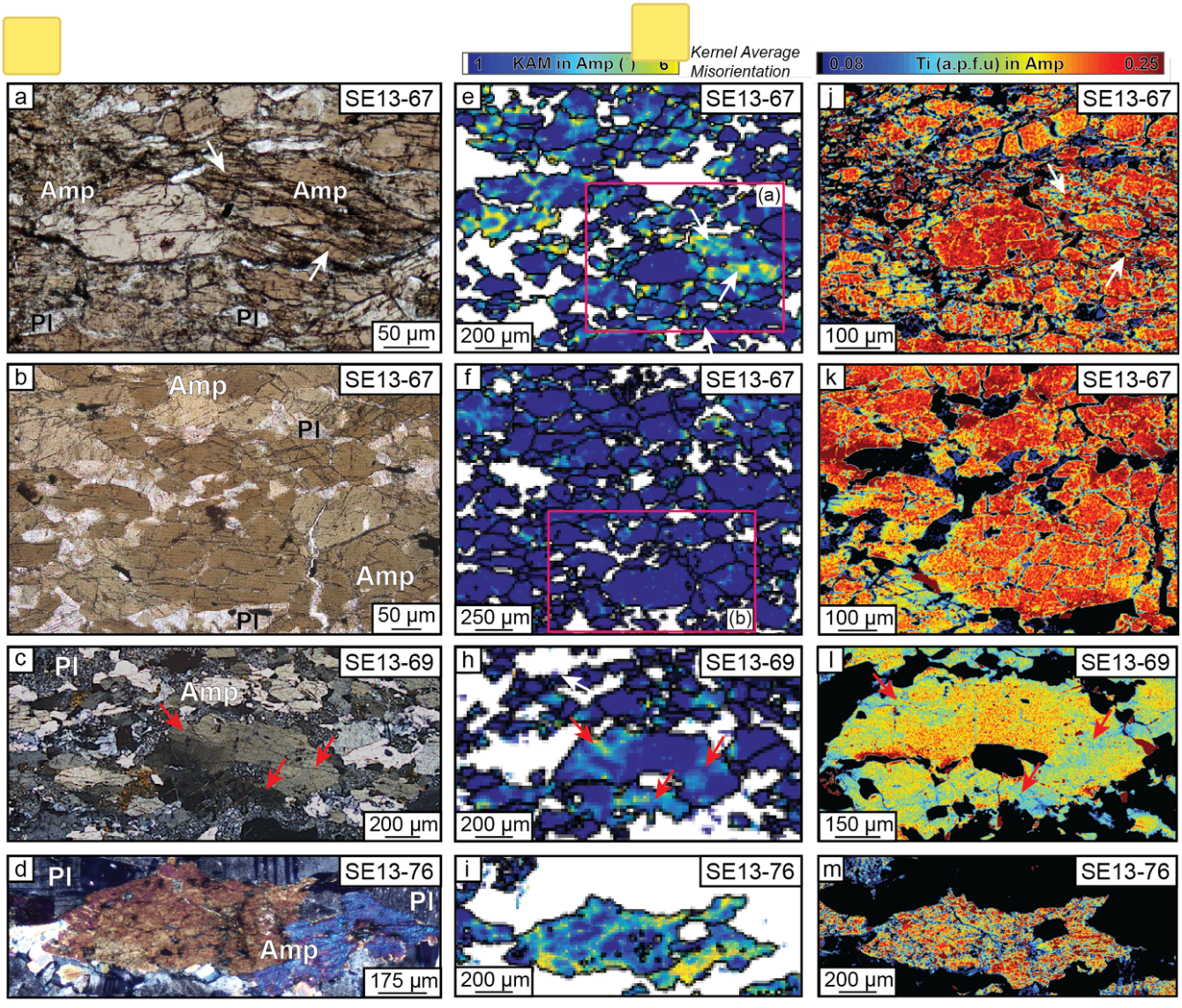

Figure 6: (a-d) Photographs of representative textures of amphibole, (e-i) [2-10°] intracrystalline misorientation (to the mean grain orientation) and (j-m) compositional map of Ti of amphibole in samples sorted in function of the distance from the peridotite.

Solid Earth Discuss., https://doi.org/10.5194/se-2019-28
Manuscript under review for journal Solid Earth
Discussion started: 14 February 2019

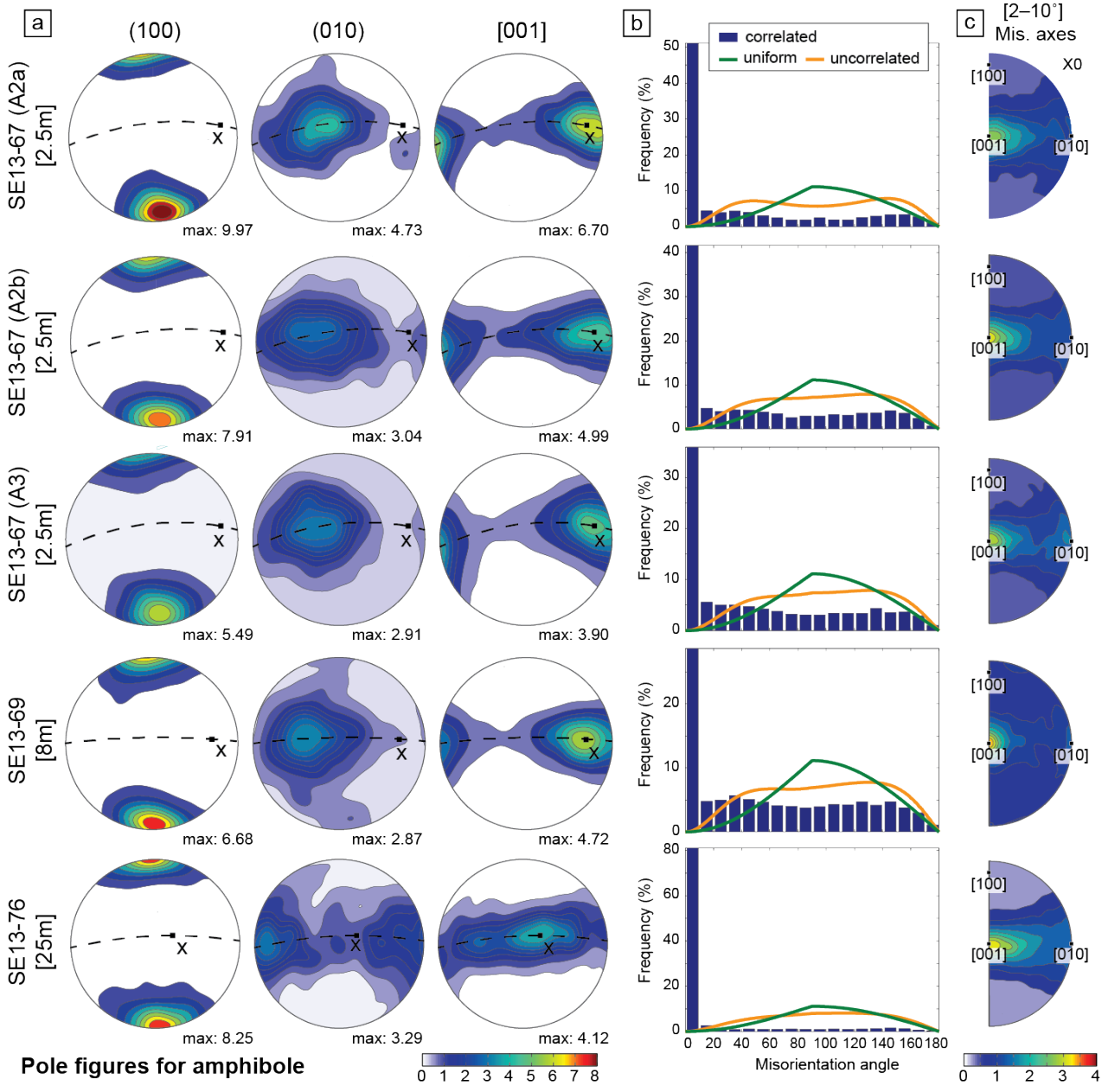

Figure 7: (a) Pole figures illustrating amphibole CPO of the samples from the HTa unit in Sumeini massif. Samples are sorted using the distance from the peridotite, with increasing distance downwards. The dashed line represents the foliation and X points to the lineation. Contours are multiples of a uniform distribution. All plots are lower hemisphere projections. Numbers in square brackets refer to the distance to the peridotite; (b) Distribution of misorientation angles between correlated (adjacent) pixels (blue histogram) and between uncorrelated pixels (orange curve) of amphibole. The uniform (green) curve corresponds to the theoretical misorientation distribution for a perfectly randomly oriented crystals; (c) Amphibole inverse pole figures showing the distribution of correlated misorientation axes (between 2° and 10°). Contours are multiples of uniform distribution.

Solid Earth Discuss., https://doi.org/10.5194/se-2019-28
Manuscript under review for journal Solid Earth
Discussion started: 14 February 2019

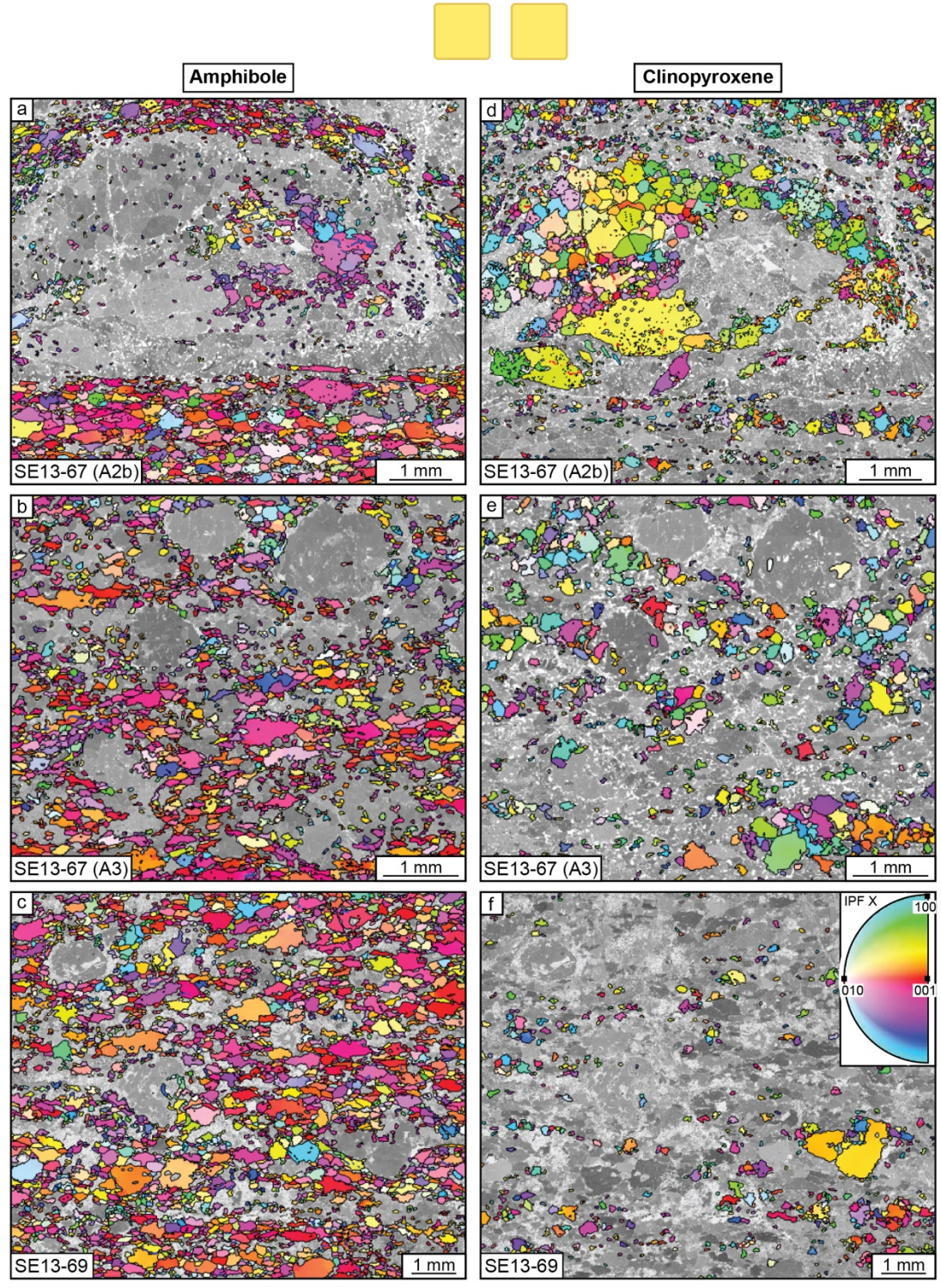

Figure 8: X direction IPF Inverse pole coloring orientation maps for (a-c) amphibole and (d-f) clinopyroxene.

Solid Earth Discuss., https://doi.org/10.5194/se-2019-28
Manuscript under review for journal Solid Earth
Discussion started: 14 February 2019

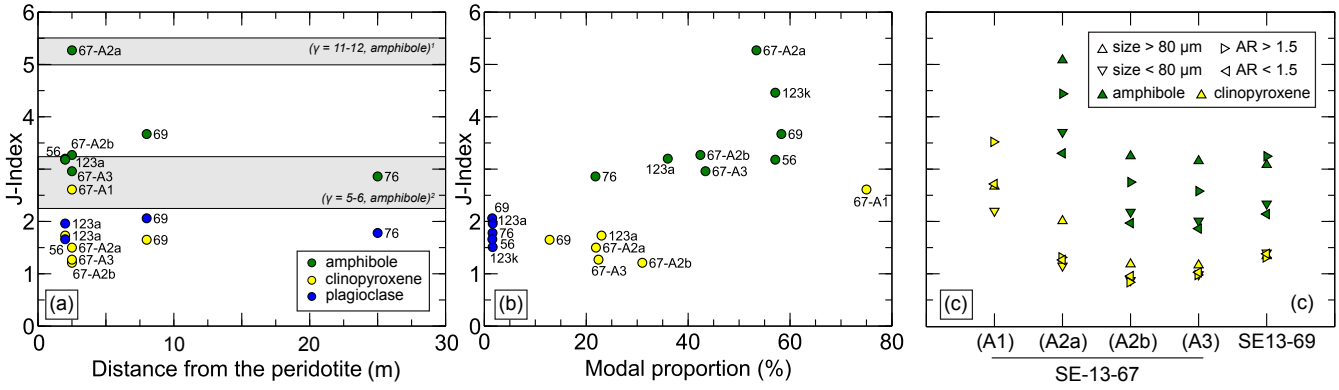

Figure 9: Quantified CPO strength (using the J-index) of amphibole, clinopyroxene and plagioclase vs. (a) the distance from the contact with the peridotite and (b) the modal proportion of each phases from Sumeini, Khubakhib and Wadi Tayin localities (see Table 1); (c) the J-index of amphibole and clinopyroxene in function of their aspect ratio and grain size for the samples from the Sumeini cross-section.

Solid Earth Discuss., https://doi.org/10.5194/se-2019-28
Manuscript under review for journal Solid Earth
Discussion started: 14 February 2019

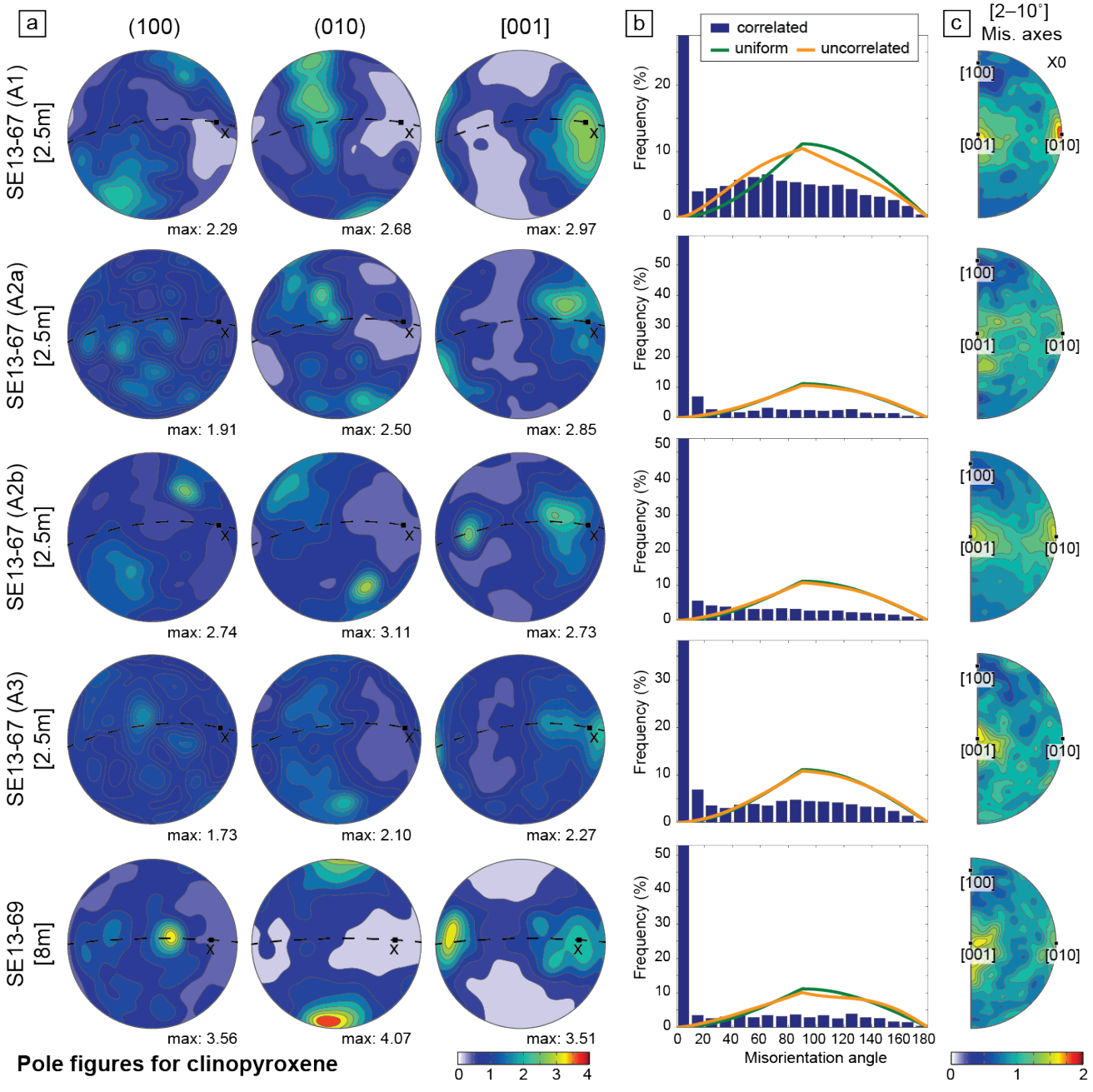

Figure 10: (a) Pole figures illustrating CPO of clinopyroxene in samples from the HTa unit of Sumeini; (b) Distribution of misorientation angles; (c) Inverse pole figures showing the distribution of correlated misorientation axes (between 2° and 10°). See caption of figure 7 for details.

Solid Earth Discuss., https://doi.org/10.5194/se-2019-28
Manuscript under review for journal Solid Earth
Discussion started: 14 February 2019

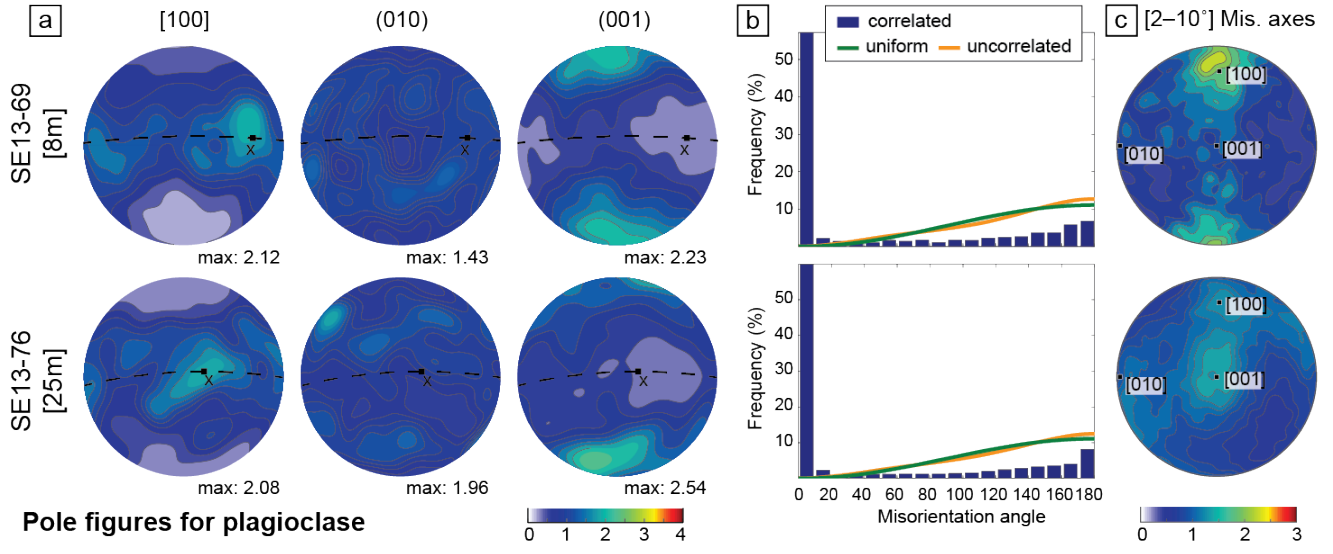

Figure 11: Pole figures illustrating CPO of plagioclase in samples from the HTa unit of Sumeini; (b) Distribution of misorientation angles; (c) Inverse pole figures showing the distribution of correlated misorientation axes (between 2° and 10°). See caption of figure 7 for details. See caption of figure 7 for details.

Solid Earth Discuss., https://doi.org/10.5194/se-2019-28
Manuscript under review for journal Solid Earth
Discussion started: 14 February 2019

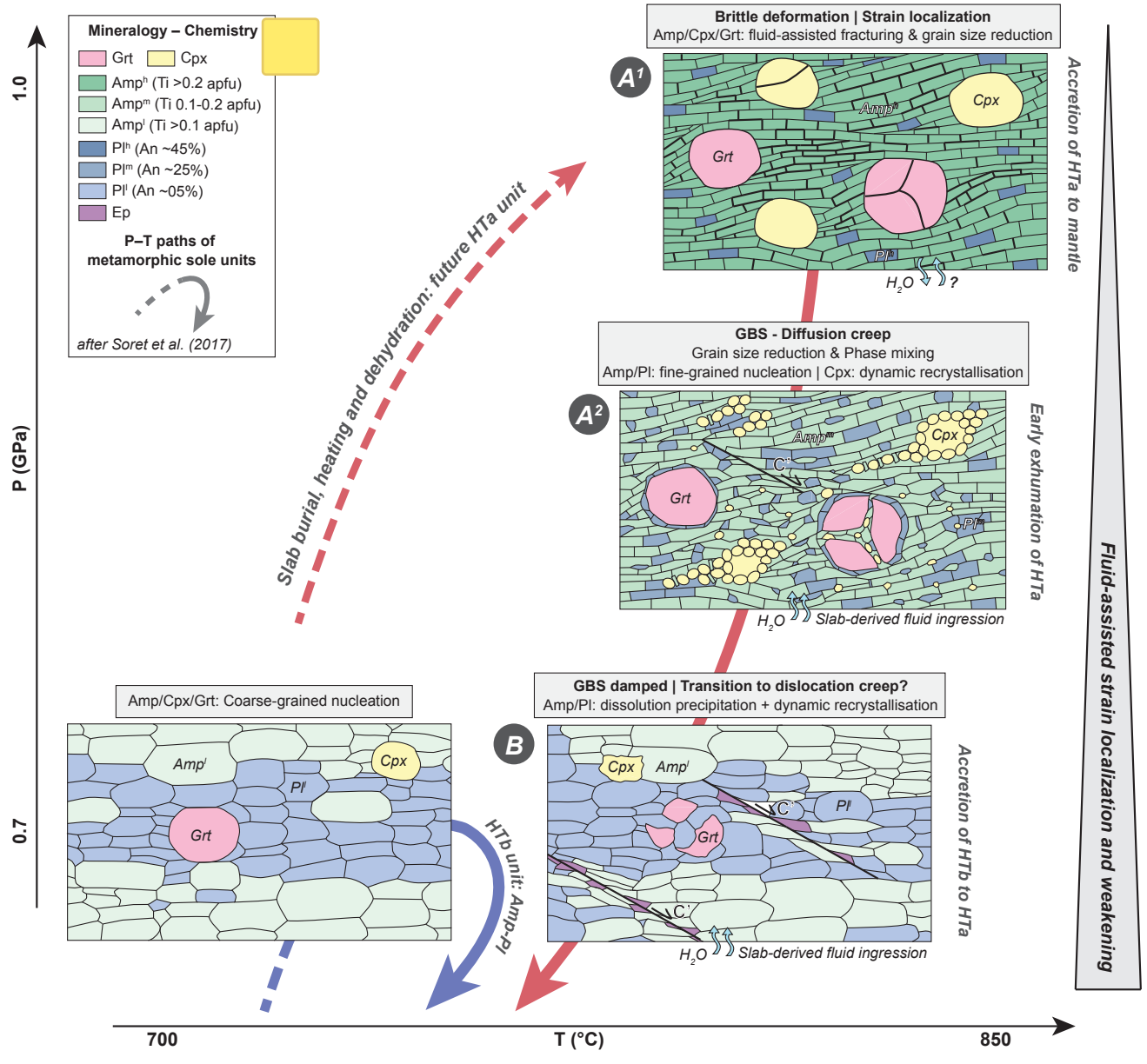

Figure 12: Model evolution at the grain-scale of the deformation of the amphibolite of the Semail metamorphic sole (as a witness of that of the top of the slab crust during subduction infancy) during the formation, accretion and early exhumation to the peridotite during the subduction infancy.

Solid Earth Discuss., https://doi.org/10.5194/se-2019-28
Manuscript under review for journal Solid Earth
Discussion started: 14 February 2019

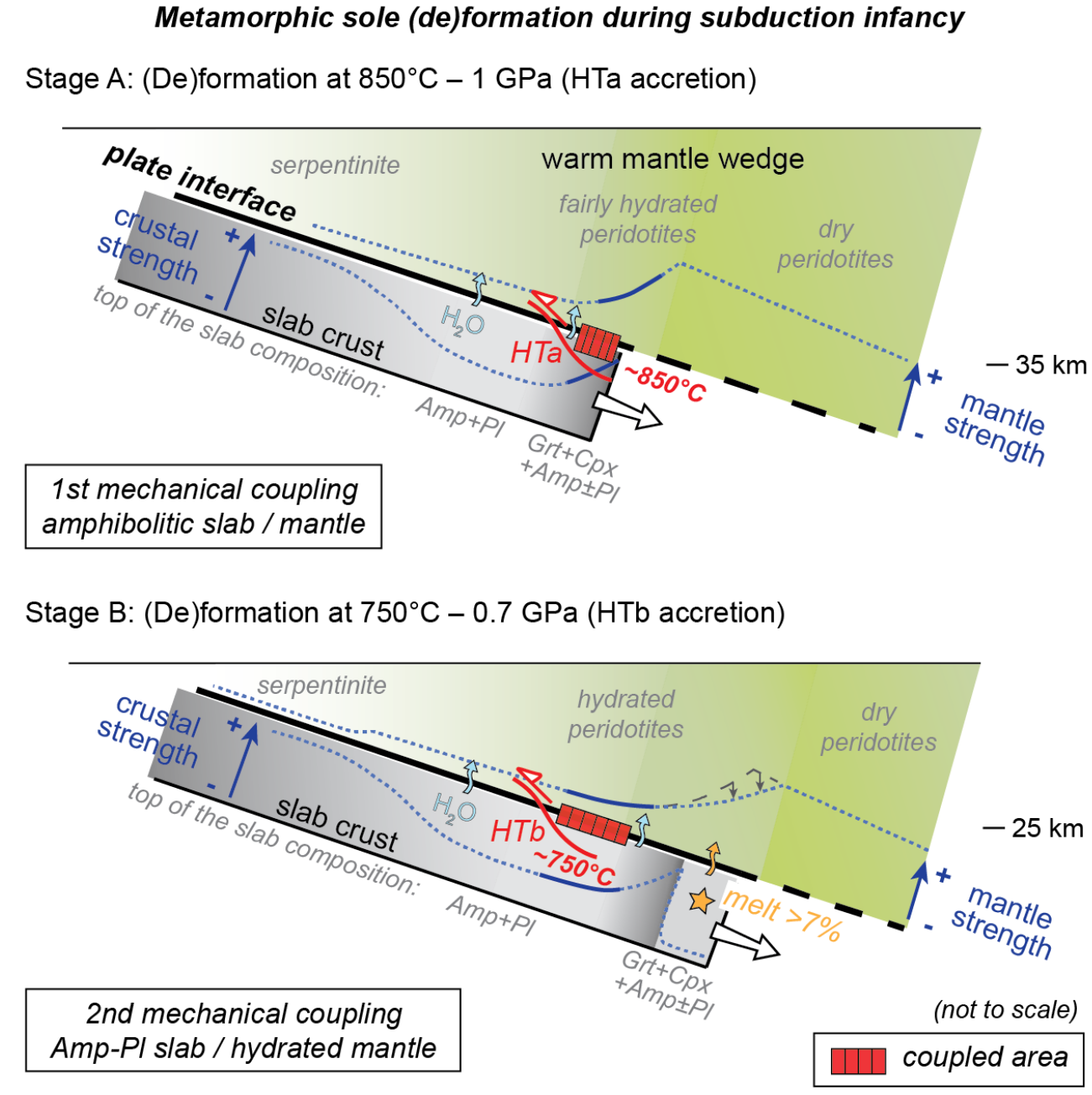

Figure 13: Schematic view of the strength evolution in the top of the slab crust and in the peridotite across the nascent subduction interface. Strong and transient interplate mechanical coupling allows the detachment and accretion of HTa and HTb metamorphic soles units to the peridotite (of the future ophiolite).

5

Solid Earth Discuss., https://doi.org/10.5194/se-2019-28
Manuscript under review for journal Solid Earth
Discussion started: 14 February 2019

Table 1. Sample location, mineral assemblage and micro-structure quantification.

Loc.	Sample (Area)	Dist. (m)	Zone	Pixel length (µm)	Phase % area					Mean [median] grain size (µm)				Mean aspect ratio				J index [M index] (1 point per grain)			Number of map grains (>10 pixels)			
					Grt	Amp	Cpx	Pl	NI	Grt	Amp	Cpx	Pl	Grt	Amp	Cpx	Pl	Amp	Cpx	Pl	Grt	Amp	Cpx	Pl
Sum.	SE13-67 (A1)	2.5	HTa	8	–	3	75	–	8	–	–	103 [31]	–	–	–	1.53	–	–	2.61 [0.099]	–	–	–	2495	–
	SE13-67 (A2a)	2.5	HTa	8	–	53	22	–	18	–	73 [56]	63 [51]	–	–	1.89	1.63	–	5.27 [0.213]	1.50 [0.015]	–	–	1817	987	–
	SE13-67 (A2b)	2.5	HTa	8	–	43	31	–	13	–	75 [57]	69 [57]	–	–	1.87	1.64	–	3.27 [0.124]	1.21 [0.011]	–	–	7305	5766	–
	SE13-67 (A3)	2.5	HTa	8	12	42	22	–	13	272 [105]	66 [55]	71 [57]	–	1.47	1.87	1.58	–	2.96 [0.114]	1.27 [0.011]	–	50	4934	2125	–
	SE13-69	8	HTa	15	3	58	13	14	9	323 [197]	116 [93]	107 [88]	93 [81]	1.39	1.81	1.57	1.54	3.67 [0.132]	1.65 [0.046]	2.06 [0.055]	33	5553	1446	2090
	SE13-76	25	HTa*	15	–	22	–	60	6	–	158 [110]	–	184 [124]	–	1.90	–	1.60	2.86 [0.086]	–	1.78 [0.033]	–	1315	–	2476
Khu.	SE13-123a	2	HTa	11	7	36	23	17	11	308 [171]	94 [68]	98 [68]	74 [59]	1.73	1.96	1.61	1.64	3.20 [0.113]	1.73 [0.042]	1.96 [0.037]	23	2202	1108	1548
	SE13-123k	40	HTb	10	9	57	–	15	6	383 [339]	130 [106]	–	79 [68]	1.49	1.82	–	1.63	4.46 [0.157]	–	1.51 [0.020]	89	5793	–	4192
WT.	SE13-56	4	HTa*	12	–	57	4	25	10	–	113 [72]	156 [97]	83 [62]	–	1.86	1.65	1.56	3.18 [0.115]	/	1.66 [0.031]	–	3478	149	2747

– : not present; NI: not indexed phase
Sum.: Sumeini; Khu.: Khubakhib; WT.: Wadi Tayin

Table 1.

Table 2. Deformation evolution of the HTa amphibolite

	A1 - HTa accretion 850°C / 1 GPa	(Fig.)	A2 - Early exhumation 850-750°C	(Fig.)	B1 - HTb accretion 700-750°C / 0.7 GPa	(Fig.)
Stable minerals	Grt + Cpx + Amph		Amp^m + Pl		Amp^I + Pl	
Garnet	Fracturing	*(5c)*	Rigid Particule Dissolution	*(3d)* *(5d)*	Absent or Trace	*(3a-d)*
Clinopyroxene	Fracturing + healing Brittle Deformation (+)	*(5h)*	Dynamic recrystallization Dissolution	*(5f-g)* *(5d)*	Absent or Trace	*(3a-d)*
Amphibole	Fracturing + healing along specific planes Brittle Deformation (+)	*(6a,b)* *(6j,k)*	GBS / Grain Rigid Rotation Fine-grained nucleation Brittle Deformation (-) Dissolution - Precipitation (+)	*(5b,d)* *(S1)* *(6c,l)*	Dissolution - Precipitation Dynamic recrystallization	*(5e)* *(6m)* *(6i)* *(7a)*
Plagioclase	Absent or Trace		Fine-grained nucleation Dissolution - Precipitation	*(6b,c)*	Dissolution - Precipitation Dynamic recrystallization	*(6m)* *(12a)*
Bulk rock amphibolite	Grain Size Reduction Fluid-assisted brittle deformation	*(3a-d)*	Phase Mixing GBS - diffusion creep	*(3a-d)* *(3d)* *(4a)*	Rock re-equilibration Transition to dislocation creep?	*(3a-d)* *(3d)* *(4a)*
Strain	Fluid-assisted strain accommodation and weakening					

Table 2.